AN EXPERIMENTAL INVESTIGATION OF HYPERSONIC FLOW OVER BLUNT NOSED CONES AT A MACH NUMBER OF 5.8

Thesis by

Reginald M. Machell

Lieutenant, U. S. Navy

In Partial Fulfillment of the Requirements

For the Degree of

Aeronautical Engineer

California Institute of Technology

Pasadena, California

1956

ACKNOWLEDGMENTS

The author wishes to express his appreciation to Professor Lester Lees for his interest and guidance during the course of this investigation. Helpful suggestions and criticisms were received from Mr. James M. Kendall and Mr. Robert E. Oliver, and their assistance is gratefully acknowledged. Sincere thanks are extended to the staff of the GALCIT hypersonic wind tunnel for their cooperation and assistance, to Mr. George Carlson of the GALCIT machine shop who skillfully constructed the models, to Mrs. Fae S. Kelley who performed many of the calculations and prepared the graphs, and to Mrs. H. Van Gieson who kindly assisted in the clerical details and typed the final manuscript.

ABSTRACT

Six spherical nosed cone static pressure models with cone semivertex angles of 10°, 20°, and 40° were tested in the GALCIT 5 x 5 inch hypersonic wind tunnel at a Mach number of 5.8. The static pressure distributions obtained at yaw angles of 0°, 4°, and 8° agreed very closely with the modified Newtonian approximation, $C_p = C_{p_{max}} \cos^2 \eta$, on the spherical portions of the models, where η is the angle between the normal to the body surface and the free stream direction. On the conical portions of the models the pressure distributions agreed reasonably well with the theoretical results for inviscid supersonic flow over cones as tabulated by Kopal. The significant parameter which influenced the deviations from the Newtonian and the Kopal predictions was the cone semivertex angle. The flow over the 40° spherical nosed cone models overexpanded with respect to the Kopal pressure in the region of the spherical-conical juncture, after which the pressure returned rapidly to the Kopal value. For models with smaller cone angles the region of minimum pressure occurred farther back on the conical portion of the model, and the Kopal pressure was approached more gradually. The shape of the pressure distributions as described in nondimensional coordinates was independent of the radius of the spherical nose and of the Reynolds number over the range of Reynolds number per inch between $.97 \times 10^5$ and 2.38×10^5. Integrated results for the pressure foredrag of the models at zero yaw compared very closely with the predictions of the modified Newtonian approximation, except for models with large cone angles and small nose radii.

TABLE OF CONTENTS

LIST OF FIGURES

LIST OF SYMBOLS

C_{D_F}	pressure foredrag coefficient, $\frac{\text{(FOREDRAG)}}{\frac{1}{2}\rho_\infty U_\infty^2 (\pi R^2)}$
C_p	pressure coefficient, $\frac{p - p_\infty}{\frac{1}{2}\rho_\infty U_\infty^2}$
$C_{p_{max}}$	pressure coefficient at forward stagnation point
p	static pressure on the surface of a model
p_∞	static pressure in the free stream ahead of the shock wave
r	radius of the spherical nose of a model
R	radius of the base of a model, .875 inches for all models
r/R	bluntness ratio of a model
S	arc length along the surface of a model, measured from the axis of symmetry
U_∞	velocity of the free stream ahead of the shock wave
α	angle of yaw
γ	ratio of specific heats
δ	shock wave separation distance from the nose of a model
η	angle between the direction of the free stream velocity and the normal to the surface of a model at any point
θ_c	semivertex angle of the conical portion of a model
ρ_∞	air density in the free stream ahead of the shock wave
ρ_2	air density behind the bow shock wave

I. INTRODUCTION

Structural problems resulting from the aerodynamic heating of slender, sharp-nosed bodies in very high speed flight may require that future hypersonic flight vehicles have blunt noses in order to provide sufficient space for heat removal apparatus. Furthermore, it has been shown by Sommer and Stark (Ref. 1), and Eggers, Resnikoff, and Dennis (Ref. 2) that for a body of revolution of a given length or volume the minimum drag at hypersonic airspeeds is obtained with a shape having a blunt nose. Hence the aerodynamics of blunt bodies in hypersonic flow is a subject of considerable current interest.

The flow over a hemisphere-cylinder has been investigated by Korobkin (Ref. 3), Stine and Wanlass (Ref. 4), Stalder and Nielsen (Ref. 5), and Oliver (Ref. 6), for supersonic Mach numbers up to 5.8. Oliver also measured the pressure distribution at zero yaw over several other blunt body shapes at a Mach number of 5.8, including a 40° half angle cone with a spherical nose. The present investigation was initiated to obtain more extensive information on hypersonic flow over blunt nosed cones at zero yaw and at small angles of yaw. In particular it was desired to find the effect on the pressure distribution and the shock wave shape of systematically varying the cone semivertex angle and the ratio of the radius of the spherical nose to the radius of the base of the cone.

Although no exact general theory exists for hypersonic flow over blunt bodies, it has been found useful to compare the results for pressure distributions over blunt bodies in hypersonic flows with a modification of Newtonian theory. (Refs. 6, 7, and 8) According to the Newtonian concept the air flowing around a body is undisturbed by the presence of the body until it strikes the solid surface, at which time the air loses the component of momentum normal to the surface. The resulting increase in pressure at the body surface is then $p - p_\infty = \rho_\infty U_\infty^2 \cos^2 \eta$, where η is the angle between the direction of the free stream velocity and the normal to the body surface; and the pressure coefficient on the surface is $C_p = 2 \cos^2 \eta$. In hypersonic flow the shock wave is wrapped closely around the body, and the Newtonian value of the surface pressure coefficient is approached as the Mach number becomes infinite and γ approaches unity. For finite Mach numbers in air the maximum pressure coefficient behind a detached bow shock wave is always less than 2.0, being 1.817 at a Mach number of 5.8, and 1.657 at a Mach number of 2.0, for $\gamma = 1.4$; therefore, it seems appropriate to modify the expression for the pressure coefficient to give $C_p = C_{p_{max}} \cos^2 \eta$, where $C_{p_{max}}$ is the pressure coefficient at the forward stagnation point. This last relation is the modified Newtonian approximation which has been used in this investigation in comparing the experimental results for the pressure distributions.

The present tests were conducted at a nominal Mach number of 5.8 in the GALCIT hypersonic wind tunnel, Leg No. 1. The experimental phase of the investigation was carried out jointly with William T. O'Bryant, Commander, U. S. Navy.

II. EQUIPMENT AND PROCEDURE

A. Description of the Wind Tunnel and Instrumentation

The GALCIT 5 x 5 inch hypersonic wind tunnel, leg no. 1, is a closed-return, continuously operating tunnel with a nominal test section Mach number of 5.8. The stagnation pressure may be varied between 14.7 and 95 psia, and the stagnation temperature may be varied between 70° and 300°F. Extensive facilities are provided for filtering and drying the air in the tunnel. Two 32-tube vacuum-referenced manometers were used to measure static pressures on the models, one manometer using mercury, and the other, DC-200 silicone fluid. A schematic diagram of the wind tunnel and compressor plant is shown in Figure 1, and a detailed description of the wind tunnel installation and the associated instrumentation is given in References 9 and 10.

B. Description of the Models

The six brass models used in the investigation are shown in Figures 2, 3, 4, and 5. The general configuration of each model was a conical section with a spherical nose. All six models had a base radius of .875 inches. Two parameters were varied in the construction of the models; the cone semi-vertex angle and the nose radius. The following combinations of these two parameters were used:

Model	Semi-vertex angle, θ_c	Nose radius, r	Base radius, R	Bluntness ratio, r/R
1	40°	.350"	.875"	.4
2	40°	.700"	.875"	.8
3	20°	.350"	.875"	.4
4	20°	.700"	.875"	.8
5	20°	.931"	.875"	1.064
6	10°	.700"	.875"	.8

The fifth model represented the maximum nose radius which could be inscribed in a 20° half angle cone having a base radius of .875 inches, and in this limiting case the geometrical shape was a simple spherical segment (Fig. 5A).

Static pressure orifices were located on the spherical and conical surfaces of each model, as shown in Figures 3, 4, and 5. These orifices, .016 inches in diameter, were drilled normal to the surface to a depth of approximately .040 inches, where they intersected larger passages drilled through the model from the rear. A typical arrangement of these internal passages is shown in Figure 6. Short lengths of stainless steel tubing were brazed into each of the holes in the rear of the model, permitting attachment of flexible saran plastic tubing which was used to connect the model to the manometers. The tubes extending from the rear of each model may be seen in Figure 2. The advantage of this type of construction was the absence of internal joints where inaccessible leaks might occur.

Two methods were used in mounting the models in the wind tunnel. For tests at zero yaw the models were mounted on an axial sting which was supported at the rear at a point well downstream of the test section and at the front by a vertical strut from the top of the test section (Fig. 7A). The distance between the forward support and the base of the model was 4½ inches. To minimize disturbances to the base pressure on the model, the pressure leads were wrapped closely around the sting for some distance downstream of the model, after which they were led out of the tunnel and connected to the manometers.

For the angle of yaw tests the models were mounted on a short sting which was supported by two vertical struts from the top of the test section (Fig. 7B). The distance between the forward support and the base of the model was 3½ inches. Differential movement of the two vertical struts by means of external controls permitted variation of the angle of yaw of the model. (Since the models were axially symmetric, the term angle of yaw as used in this discussion is synonymous with the term angle of attack.)

In both methods of mounting, the model was attached to the sting by means of a close fitting shaft and sleeve, which were machined true with the axis of the model (Fig. 6). This arrangement permitted the models to be rotated about their axes without changing the angle of yaw. A set screw maintained the models in any desired rotational position.

C. Test Procedure

All six models were tested at zero yaw, and Models 1 and 4 (Figs. 3A and 4B) were tested at angles of yaw of 4° and 8°.

For the tests at zero yaw the models were positioned on the tunnel axis. The nose of each model was located 24 inches downstream of the throat. After the pressure leads were connected to the manometers the system was checked for leaks. The tunnel was operated for at least 90 minutes before data was taken in order to allow equilibrium temperatures to be reached throughout the wind tunnel and the compressor plant. Static pressure measurements were made at a stagnation pressure of 75 psia and a stagnation temperature of 225°F., which corresponded to free stream conditions of a Mach number of 5.8 and a Reynolds number per inch of 1.91×10^5. Empty tunnel pressure surveys by previous investigators had shown a variation of total pressure up to plus or minus three per cent in the region of the tunnel used for these tests; therefore, data was taken in three rotational positions of each model spaced 90° apart around the axis of revolution.

For the tests at angles of yaw the models were initially positioned on the tunnel axis with the nose of each model located at approximately $21\frac{1}{2}$ inches downstream of the throat. Leak checks were conducted as before. The models were yawed by differential movement of the vertical supports in such a manner as to keep the nose of the model on the tunnel centerline at all times. Static pressure measurements were made at angles of yaw of 0°, 4°, and 8°, at a stagnation pressure of 95 psia and a stagnation temperature of 225°F. These stagnation conditions corresponded to free stream conditions of a Mach number of 5.8 and a Reynolds number per inch of 2.38×10^5. As shown in Figures 3A and 4B the pressure orifices were located in four meridian planes, 45° apart, through the axes of the models. When a model was mounted in the tunnel, one of the meridian planes of the model which contained the pressure orifices was aligned vertically. This meridian plane was designated as the vertical meridian plane, and this was the plane in which the model was yawed. The meridian planes containing the other pressure orifices on the model were designated as the diagonal meridian planes and the horizontal meridian plane. For each model at a given angle of yaw it was desired to obtain pressure measurements at every orifice location in each of the four meridian planes. This aim was accomplished by taking pressure readings with the model yawed first above and then below the free stream direction in each of five rotational positions, separated by 45°. Because of the axial symmetry, this procedure was equivalent to taking measurements in ten rotational positions of each model at each angle of yaw.

In order to investigate the effect of Reynolds number variation, Model 4 was also tested at zero yaw at stagnation pressures of 37 psia and 54 psia at a stagnation temperature of 225°F. Free stream conditions were Reynolds numbers per inch of $.97 \times 10^{5}$ and 1.41×10^{5} respectively, and a Mach number of 5.7. These tests were identical to the previously described tests at zero yaw, except that the model was mounted on the two vertical supports, placing the nose of the model at $21\frac{1}{2}$ inches downstream of the throat.

III. RESULTS AND DISCUSSION

A. Schlieren Observations

Schlieren photographs of the flow over each of the six models at zero yaw are shown in Figures 8 through 13. For this series of observations the free stream conditions were a Mach number of 5.8 and a Reynolds number per inch of 1.91×10^5, with the exception of Figure 10, for which the Mach number was 5.7 and the Reynolds number per inch was $.97 \times 10^5$. In general it may be seen that the shock waves lie close to the bodies as is characteristic in hypersonic flow. The shape of the shock waves for the more blunt models, such as Model 4 (Fig. 11), is dominated by the effect of the blunt nose, whereas for the more pointed models, such as Model 1 (Fig. 8), the shock shape is dominated by the conical portion of the model. A peculiarity which is particularly apparent in Figure 8 and shows slightly in Figure 9 is the reverse curvature in the shock wave midway out on the conical portions of Models 1 and 2. This condition was observed only on these two 40° half angle models, and it was closely connected with the over-expansion and recompression on the conical portions of these models (see discussion of static pressure measurements at zero yaw).

The separation distance, δ, of the bow shock wave from the nose of each model at zero yaw, as measured from the schlieren photographs, is compared with the radius of the spherical nose of the model in the following table:

Model	δ, inches	r, inches	δ/r
1	.0594	.350	.169
2	.1153	.700	.165
3	.0592	.350	.169
4	.1121	.700	.160
5	.1496	.931	.161
6	.1098	.700	.157
		Average =	.164

From this table it is apparent that the variation of shock separation distance with the radius of the nose of the model was essentially linear. Theoretical analyses have been made by Heybey (Ref. 11), Hayes (Ref. 12), and Li and Geiger (Ref. 13) to predict the bow shock wave separation distance for blunt bodies in hypersonic flow. Heybey's analysis gives the shock separation distance in front of a sphere at a Mach number of 5.8 as $\delta/r = .138$, including the correction for compressible flow behind the bow shock. Hayes' analysis, which assumes the density ratio across the bow shock wave, ρ_∞/ρ_2, to be very small and also assumes incompressible flow behind the shock, gives a value of $\delta/r = .118$. The analysis by Li and Geiger, which again assumes a very small density ratio and incompressible flow behind the shock, predicts a value of $\delta/r = .137$ for the conditions of the present experiment. Since the density ratio across a bow shock wave at a Mach number of 5.8 is .192, which is not very small with respect to 1.0, the agreement between the present results and the foregoing theoretical predictions is considered fair.

The schlieren photographs of Models 1 and 4 at angles of yaw of 4° and 8° are shown in Figures 14 through 17. For these observations the free stream conditions were a Mach number of 5.8 and a Reynolds number per inch of 2.38×10^5. The shock wave shapes for the yawed models were generally quite similar to those for the same models at zero yaw, except for the slight asymmetry introduced by the angle of yaw.

B. Static Pressure Measurements at Zero Yaw

The pressure distributions at a Mach number of 5.8 and a Reynolds number per inch of 1.91×10^5 for each of the six models at zero yaw are plotted in Figures 18 through 23 in the form $C_p/C_{p_{max}}$ versus S/r, where S is the arc length along the surface of the model measured from the axis of symmetry, and r is the radius of the spherical nose of the model. Along the spherical surface S/r corresponds to the polar angle in radians, and along the conical surface S/r corresponds to a dimensionless linear distance. In obtaining these results for $C_p/C_{p_{max}}$ the three sets of pressure data for each model were reduced separately and then averaged to give a mean value for the pressure coefficient at each orifice location on the model. Also plotted in Figures 18 through 23 are the values for $C_p/C_{p_{max}} = \cos^2 \eta$ based on the modified Newtonian approximation. For the conical portions of the models the values of $C_p/C_{p_{max}}$ computed from the Kopal tables (Ref. 14) for inviscid supersonic flow over cones are shown for comparison.

The pressure distribution on Model 1, $\theta_c = 40^\circ$, (Fig. 18) followed the modified Newtonian approximation very closely on the spherical portion of the model. On the conical portion the pressure followed the Newtonian prediction for a short distance and then increased to the Kopal value. In effect the air flowing around the junction of the spherical and the conical portions of the model, which is called the shoulder of the model in this discussion, overexpanded and then was recompressed to the equilibrium cone value. This appreciable over-expansion below the Kopal pressure at the shoulder occurred only on the 40° models. On Model 2, $\theta_c = 40^\circ$, the pressure distribution (Fig. 19) followed the Newtonian value very closely over the entire model. The shape of the pressure distribution curve for Model 2 was nearly identical to that for Model 1 over the region of comparison in the coordinate S/r, and this similarity is shown in Figure 24, in which the results for Models 1 and 2 are replotted. This very close similarity indicates that the variation of the bluntness ratio, r/R, had no effect on the unyawed pressure distribution on this family of models, when the pressure distribution was described with respect to the nondimensional coordinate S/r.

On Model 3, $\theta_c = 20^\circ$, the pressure distribution (Fig. 20) followed the modified Newtonian approximation very closely on the spherical portion until just ahead of the juncture of the conical section. At the shoulder the pressure was slightly above the Kopal value, and along the conical portion the pressure decreased gradually to the Newtonian value. There is some evidence of a pressure minimum well back on the conical portion of the model. In Figures 21 and 22 the pressure distributions for Models 4 and 5, $\theta_c = 20^\circ$, may be seen to be nearly identical to the result obtained on Model 3, within the region of comparison. The pressure data for these three models is replotted in Figure 25, where the very close similarity in the results for all three models is clearly apparent. Just as for Models 1 and 2 the variation of bluntness ratio, r/R, for this second family of models had no effect on the shape of the pressure distribution at zero yaw, when the pressure data was described with respect to the nondimensional coordinate S/r.

Figure 21 also shows the experimental results for the surface pressure on Model 4 for three other test conditions corresponding to Reynolds numbers per inch of 0.97×10^5 and 1.41×10^5 at a Mach number of 5.7, and a Reynolds number per inch of 2.38×10^5 at a Mach number of 5.8. The close agreement of the results for these four test conditions indicates that the variation of Reynolds number over this range had no appreciable effect on the pressure distribution over the model. This indication is also borne out by the comparison of the results for Models 1 and 2, and Models 3 and 4. Both of these pairs of models had a variation in nose radius by a factor of two, corresponding to a variation of Reynolds number based on nose radius between $.67 \times 10^5$ and 1.34×10^5, and the similarity of the pressure distribution within these two families of models again indicates the lack of Reynolds number dependence over the range of test Reynolds numbers. This similarity within the two families of models also indicates that end effects, such as pressure feed-up from the base of the model, were essentially negligible.

The pressure distribution on Model 6, $\theta_c = 10^o$, shown in Figure 23, followed the modified Newtonian approximation fairly closely up to the region just ahead of the shoulder. At the shoulder the pressure was nearly twice the Kopal pressure, and although the pressure decreased over the conical portion, it remained above the Kopal value over the entire model. Examination of this model on an optical comparator at high magnification indicated that the radius of curvature was not actually discontinuous at the shoulder, and it is believed that this slight geometrical deviation caused the pressure distribution to depart from the Newtonian value before the end of the spherical portion and raised the pressure level slightly over the remainder of the model.

Comparison of the results for Models 1, 3, and 6 (Figs. 18, 20, and 23) illustrates the effect of the cone semivertex angle, θ_c, on the shape of the pressure distribution over the conical portions of the models. For large cone angles, such as $\theta_c = 40^\circ$, the flow around the shoulder of the model overexpanded and then was recompressed fairly rapidly to the Kopal pressure. As the cone angle was decreased the pressure at the shoulder increased with respect to both the Newtonian and the Kopal values, and the region of minimum pressure moved farther back on the conical portion. For small cone angles, such as $\theta_c = 10^\circ$, the pressure at the shoulder was appreciably higher than the Kopal value, and along the conical portion of the model the pressure approached this value very gradually.

C. Static Pressure Measurements at Angles of Yaw of 4° and 8°

The results of the static pressure measurements at a Mach number of 5.8 and a Reynolds number per inch of 2.38×10^5 on Models 1 and 4 at an angle of yaw of 8° are plotted in Figures 26 through 31 in the form of $C_p/C_{p_{max}}$ versus S/r, as before. Since the results for the 4° angle of yaw contained no additional information, this data is not shown. In obtaining the results for the tests at angles of yaw, the data recorded for the different rotational positions of each model was reduced separately and then combined to give a value for the pressure coefficient at each orifice location in each of the four meridian planes of the model. Symmetry of the flow with respect to the vertical meridian plane was assumed, hence the results for the two diagonal meridian planes were averaged to give a single set of mean values for the diagonal planes. Similarly the results for the two halves of the horizontal meridian plane were averaged together. In the graphical representation the upper halves of the vertical and the diagonal meridian planes refer to the top half of the model when it is considered at a positive angle of yaw (identical to a positive angle of attack) with respect to the flow direction. In addition to the experimental results, Figures 26 through 31 show the values of $C_p/C_{p_{max}} = \cos^2 \eta$ given by the modified Newtonian approximation and also for the conical portions the values of $C_p/C_{p_{max}}$ computed using the Kopal tables (Ref. 15) for the first order theory of inviscid supersonic flow over cones at small angles of yaw.

Figures 26, 27, and 28 show the surface pressure distribution for Model 1 at $\alpha = 8^o$, for the vertical, the diagonal, and the horizontal meridian planes respectively. In all four meridian planes the pressure distribution on the spherical portion of the model followed the modified Newtonian theory very closely. In all planes the pressure at the shoulder was lower than the Kopal first order value, indicating the same over-expansion which occurred on this model at $\alpha = 0^o$. Over the conical portion the pressure rose above the Kopal pressure, particularly on the lower half of the model. The pressure distributions in the four meridian planes of Model 1 at $\alpha = 8^o$ are replotted in Figure 32 for comparison. This presentation shows more clearly the similarity in the shape of the pressure distribution in all meridian planes on the model, even though the horizontal and the diagonal meridian planes no longer coincided with streamlines when the model was yawed. The stagnation point was in the lower half of the vertical meridian plane, and it may be seen that the point at which $C_p/C_{p_{max}} = 1$ was located at an S/r of approximately 0.14, which was numerically equal to the 8^o angle of yaw expressed in radians. The horizontal and the diagonal meridian planes had maximum values of $C_p/C_{p_{max}}$ less than one, since these meridians did not pass through the stagnation point.

Figures 29, 30, and 31 show the surface pressure distribution on Model 4 at $\alpha = 8^o$, for the vertical, the diagonal, and the horizontal meridian planes respectively. Here again the pressure coefficient on the spherical portion followed the $C_{p_{max}} \cos^2 \eta$ relation very closely in all four meridian planes, up to the region of the shoulder. The pressure in this region was slightly above the Kopal value in all planes; however, on the lower half of the model the pressure then decreased to approximately the Kopal value on the conical portion, whereas on the upper half of the model the pressure remained above the first order inviscid cone theory all the way to the end of the model.

Figure 33 shows the pressure distribution in the vertical meridian plane of Model 1 at angles of yaw of 0^o, 4^o, and 8^o. These three curves show the similarity in the results at the three angles of yaw, and it is apparent that the effects of angle of yaw were essentially linear up to 8^o. As the angle of yaw was increased, the pressure on the conical portion returned more rapidly to the Kopal value on the lower half of the model, and returned more slowly to the Kopal value on the upper half of the model. If the angle of yaw is considered as a change in the effective cone angle, then for a given angle of yaw the effective cone angle would be increased on the lower half and decreased on the upper half. This consideration would indicate that a decrease in the half angle of the cone caused the region of minimum pressure to move farther back on the conical portion, and caused the pressure on the conical portion to approach the inviscid theoretical cone value more gradually. This indication agrees with the results of the tests at zero yaw, as previously discussed.

In Figure 34 the pressure data for the vertical meridian planes of both Models 1 and 4 at $\alpha = 8^{\circ}$ is replotted for comparison. This presentation shows that the pressure distribution over the spherical portion of these two models was nearly identical even though the models had different cone angles and bluntness ratios. If the yaw angle is again considered as a change in the effective cone angle, this figure again shows that as the cone angle was decreased the pressure on the conical portions of the models approached the Kopal pressure more gradually. In particular it may be seen that the pressure distribution on the upper half of Model 1, for which the effective cone angle was 32°, resembled the pressure distribution on the lower half of Model 4, for which the effective cone angle was 28°. Also the pressure distribution on the upper half of Model 4, for which the effective cone angle was 12°, had much the same characteristics as the pressure distribution on the 10° model at zero yaw (Fig. 23). These comparisons show that in the vertical meridian plane a change in the angle of yaw of the models, up to angles of 8°, was similar in effect to a change in the effective cone angle, such that as the cone angle was reduced the region of minimum pressure moved back on the conical portion and the pressure approached the Kopal pressure more gradually.

D. Drag Calculations at Zero Yaw

The pressure distributions for each of the six models at zero yaw were integrated to obtain the pressure drag on the spherical and conical portions of the models. The results are plotted in Figure 35 in the form of the foredrag coefficient referred to the base area, C_{D_F}, versus the bluntness ratio, r/R, with the cone semivertex angle as a parameter. Also shown for comparison are the foredrag coefficients for 10°, 20°, and 40° spherical nosed cones computed from the modified Newtonian approximation. For the relation $C_p = C_{p_{max}} \cos^2 \eta$, the foredrag coefficient of any spherical nosed cone is given by the formula

$$C_{D_F} = C_{p_{max}} \left[\tfrac{1}{2} \cos^4 \theta_c \, (r/R)^2 + \sin^2 \theta_c \right] .$$

In addition the foredrag coefficients are shown for 10°, 20°, and 40° semivertex angle cones as computed from the Kopal tables (Ref. 14), as well as the foredrag coefficient of a hemisphere-cylinder as computed from the data of Reference 6. Except for models with large cone angles and small bluntness ratios, the pressure drag of all the spherical nosed cones was given very closely by the modified Newtonian approximation. For large cone angles combined with large bluntness ratios, such as $\theta_c = 40°$, $r/R = 0.8$, the pressure drag of the spherical nosed cone was greater than the drag of the hemisphere-cylinder.

IV. CONCLUSIONS

On the basis of the foregoing results it was concluded that for the range of conditions of the present investigation the pressure distributions over spherically blunted cones at zero yaw and at small angles of yaw agreed very closely with the modified Newtonian approximation, $C_p = C_{p_{max}} \cos^2 \eta$, on the spherical portions. On the conical portions the pressure distributions agreed reasonably well with the theoretical results for inviscid supersonic flow over cones as tabulated by Kopal. The only factor which influenced the deviations from the Newtonian and the Kopal predictions was the semivertex angle of the conical portion. For large cone half angles, of the order of 40°, there was a marked overexpansion with respect to the inviscid cone theory value in the region of the juncture of the conical and the spherical portions of the model, but the pressure returned fairly rapidly to the inviscid theory value on the conical portion. As the cone angle was decreased the pressure at the spherical-conical juncture increased with respect to the Kopal prediction; the region of minimum pressure occurred farther back on the conical portion; and the pressure on the conical portion approached the Kopal value much more gradually. The effects of angles of yaw on the pressure distributions were linear up to yaw angles of 8°, and in the vertical meridian plane the effect of an angle of yaw was similar to the effect of a change in the semivertex angle of the conical portion of the model. Variation of the ratio of the nose radius to the base radius produced no effect on the shape of the pressure distribution when described in nondimensional coordinates.

There was no noticeable effect of Reynolds number on the pressure distribution over the range of conditions tested.

Schlieren observations showed that for the more blunt models the shock wave shape was dominated by the effects of the blunt nose, whereas for the more pointed models the shock shape was dominated by the conical portion of the model. The separation distance of the shock wave from the nose of the models at zero yaw varied linearly with the radius of the spherical nose of the model.

Drag coefficients obtained by integrating the unyawed pressure distributions for each of the models compared very closely with the predictions of the modified Newtonian approximation, except for models with large cone angles and small nose radii.

REFERENCES

1. Sommer, S. C., and Stark, J. A.: The Effect of Bluntness on the Drag of Spherical-Tipped Truncated Cones of Fineness Ratio 3 at Mach Numbers 1.2 to 7.4. NACA RM A52B13, April, 1952.

2. Eggers, A. J., Resnikoff, M. M., and Dennis, D. H.: Bodies of Revolution Having Minimum Drag at High Supersonic Airspeeds. NACA TN 3666, February, 1956.

3. Korobkin, I.: Local Flow Conditions, Recovery Factors, and Heat-Transfer Coefficients on the Nose of a Hemisphere-Cylinder at a Mach Number of 2.8. NAVORD Report 2865, May, 1953.

4. Stalder, J. R., and Nielsen, H. V.: Heat Transfer from a Hemisphere Cylinder Equipped with Flow Separation Spikes. NACA TN 3287, September, 1954.

5. Stine, H. A., and Wanlass, K.: Theoretical and Experimental Investigation of Aerodynamic-Heating and Isothermal Heat-Transfer Parameters on a Hemispherical Nose with Laminar Boundary Layer at Supersonic Mach Numbers. NACA TN 3344, December, 1954.

6. Oliver, R. E.: An Experimental Investigation of Flow over Simple Blunt Bodies at a Nominal Mach Number of 5.8. GALCIT Memorandum No. 26, June, 1955.

7. Penland, J. A.: Aerodynamic Characteristics of a Circular Cylinder at Mach Number 6.86 and Angles of Attack up to 90°. NACA RM L54A14, March, 1954.

8. Lees, L.: Hypersonic Flow. Institute of the Aeronautical Sciences, Preprint No. 554, June, 1955.

9. Eimer, M., and Nagamatsu, H. T.: Direct Measurement of Laminar Skin Friction at Hypersonic Speeds. Appendix A. GALCIT Memorandum No. 16, July, 1953.

10. Baloga, P. E., and Nagamatsu, H. T.: Instrumentation of GALCIT Hypersonic Wind Tunnels. GALCIT Memorandum No. 29, July, 1955.

11. Heybey, W. H.: Shock Distances in Front of Symmetrical Bodies. NAVORD Report 3594, December, 1953.

12. Hayes, W. D.: Some Aspects of Hypersonic Flow. Ramo-Wooldridge Corp., January, 1955.

13. Li, T. Y., and Geiger, R. E.: Stagnation Point of a Blunt Body in Hypersonic Flow. Institute of the Aeronautical Sciences, Preprint No. 629, January, 1956.

14. Staff of the Computing Section, Center of Analysis, Massachusetts Institute of Technology, under the direction of Zdenek Kopal: Tables of Supersonic Flow Around Cones. Technical Report No. 1, 1947.

15. Staff of the Computing Section, Center of Analysis, Massachusetts Institute of Technology, under the direction of Zdenek Kopal: Tables of Supersonic Flow Around Yawing Cones. Technical Report No. 3, 1947.

APPENDIX

ACCURACY ANALYSIS

In order to estimate the accuracy of the present results, the following possible sources of error were considered:

(1) Error in the angle of yaw of the model

(2) Error in aligning the pressure orifices in the desired meridian plane

(3) Variation in the flow conditions across the test section

(4) Variation in the tunnel stagnation pressure

(5) Errors in location of the static pressure orifices on the model

(6) Variation in pressure across the static pressure orifices

(7) Random errors in the manometer readings

The effects of the first three items were minimized by the procedure of taking data in several rotational positions of the model, and it was therefore assumed that these effects were negligible. The tunnel stagnation pressure was controlled within 0.5 per cent. The effects of errors in location of the static pressure orifices due to machining tolerances were estimated as less than 0.5 per cent of the pressure at the forward stagnation point, p_{max}, on Models 1 and 3, and less than 0.3 per cent of p_{max} on the other models with larger nose radii. The variation of the static pressure across the pressure orifices was as much as 5 per cent of p_{max} on the spherical portions of Models 1 and 3, and as much as $2\frac{1}{2}$ per cent of p_{max} on the spherical portions of the other models. It was assumed that the pressure registered on the manometer differed by a negligible amount from the actual static pressure at the center of the corresponding pressure orifice. This assumption appears reasonable in view of the close agreement of the results for the spherical portions of all the models tested. Random errors in the manometer readings for the static pressure on the models were estimated as 0.3 per cent of p_{max}. The magnitude of the possible error in the computed values of $C_p/C_{p_{max}}$ based on these estimated errors was plus or minus 0.012.

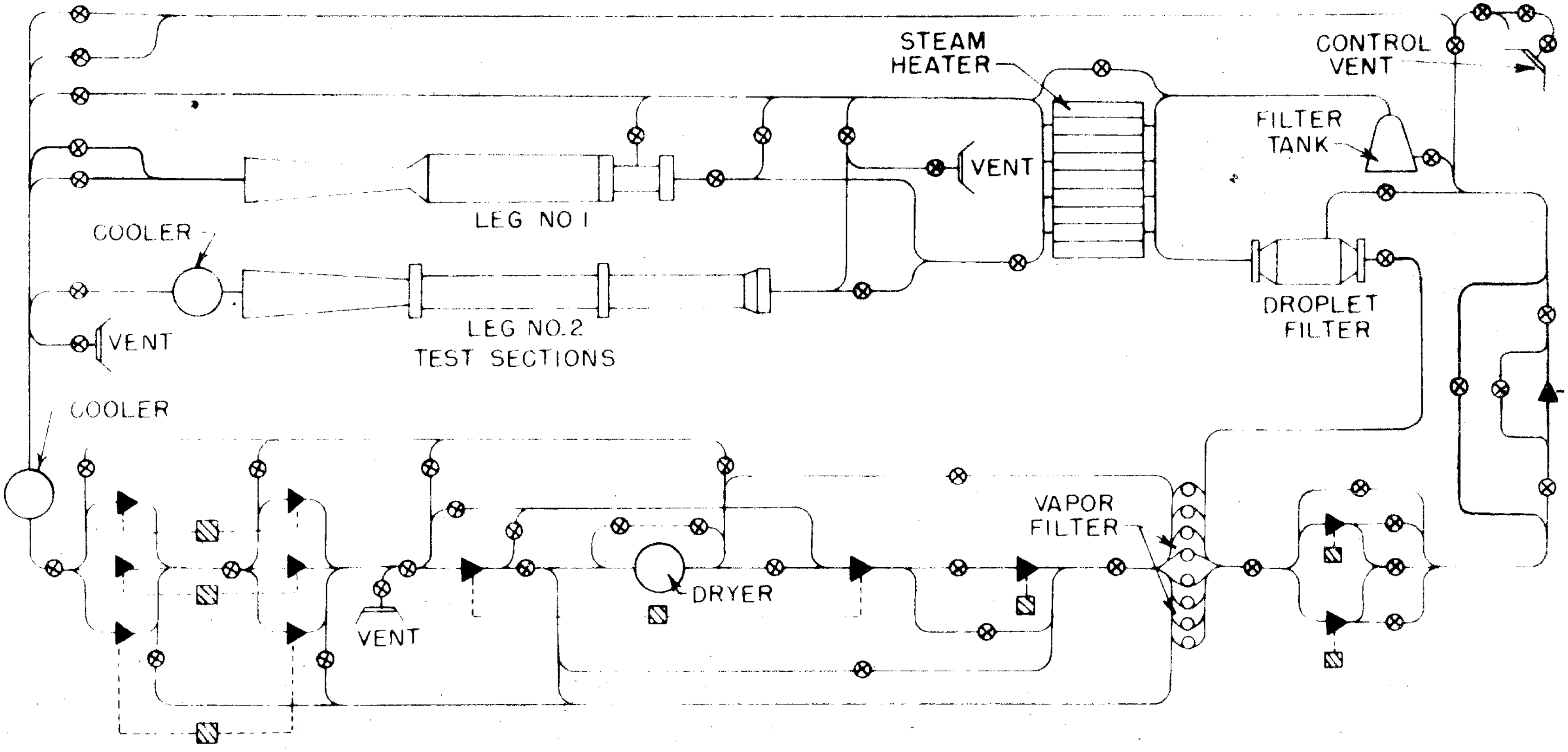

SCHEMATIC DIAGRAM

OF GALCIT 5x5in. HYPERSONIC WIND TUNNEL INSTALLATION

FIG. I

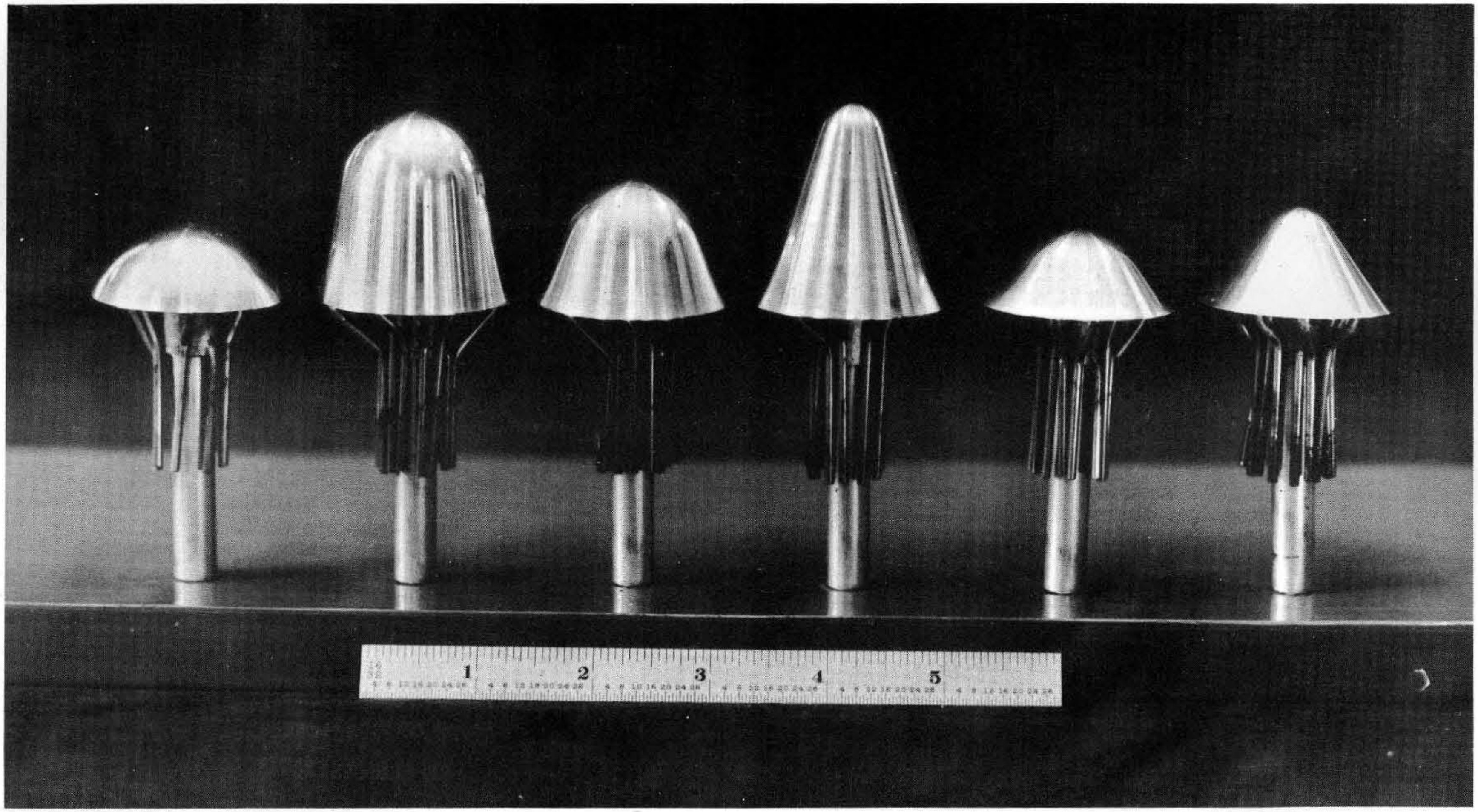

FIG. 2

SPHERICAL NOSED CONE STATIC PRESSURE MODELS

Orifice	S(in.)
1	0
2	0.070
3	0.105
4	0.140
5	0.210
6	0.210
7	0.280
8	0.315
9	0.350
10	0.385
11	0.420
12	0.490
13	0.630
14	0.805
15	0.980
16	1.155

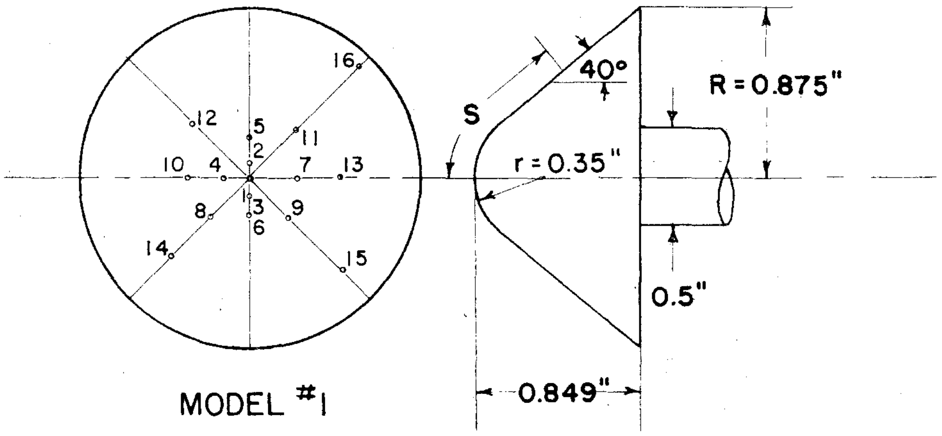

(A) 40° HALF ANGLE CONE

r/R = 0.4

Orifice	S(in.)
1	0
2	0.070
3	0.140
4	0.210
5	0.280
6	0.420
7	0.420
8	0.560
9	0.630
10	0.700
11	0.770
12	0.840
13	0.980

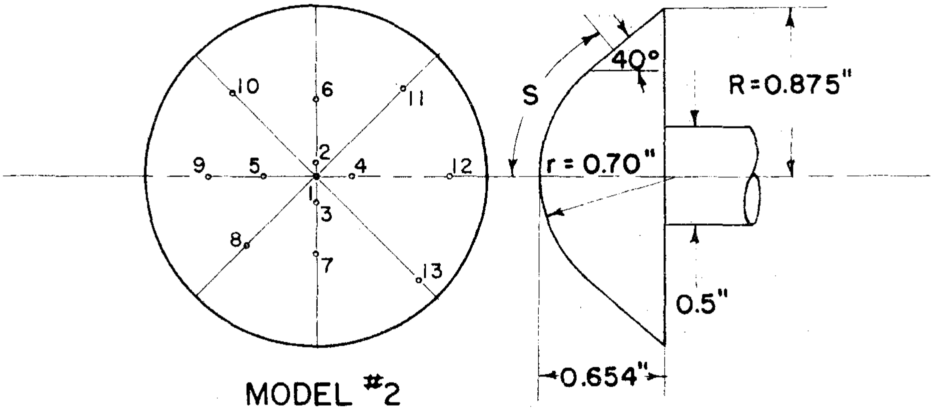

(B) 40° HALF ANGLE CONE

r/R = 0.8

FIG. 3

Orifice	S(in.)
1	0
2	0.105
3	0.175
4	0.280
5	0.385
6	0.490
7	0.595
8	0.735
9	0.735
10	0.875
11	1.155
12	1.435
13	1.715

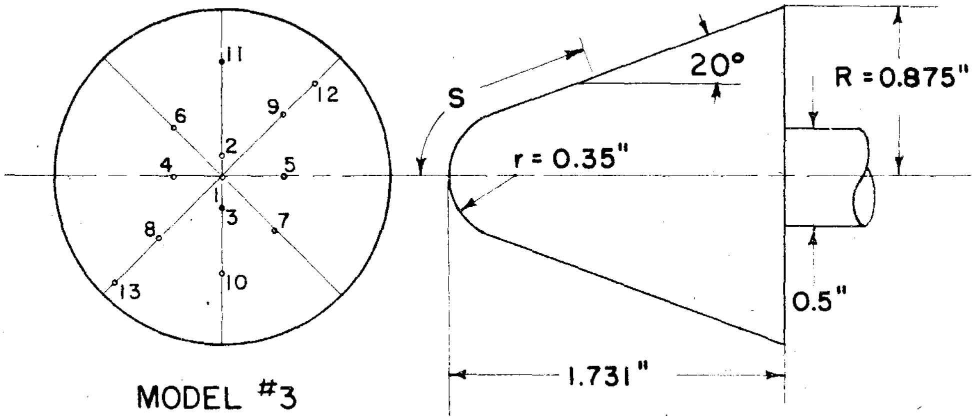

(A) 20° HALF ANGLE CONE

r/R = 0.4

Orifice	S(in.)
1	0
2	0.070
3	0.140
4	0.210
5	0.280
6	0.490
7	0.490
8	0.700
9	0.840
10	0.910
11	0.980
12	1.050
13	1.120
14	1.260

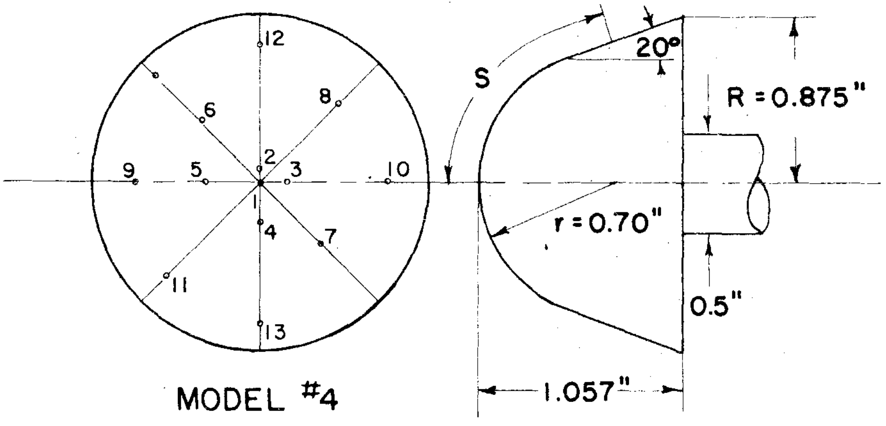

(B) 20° HALF ANGLE CONE

r/R = 0.8

FIG. 4

Orifice	S(in.)
1	0
2	0.093
3	0.186
4	0.279
5	0.372
6	0.650
7	0.650
8	0.931

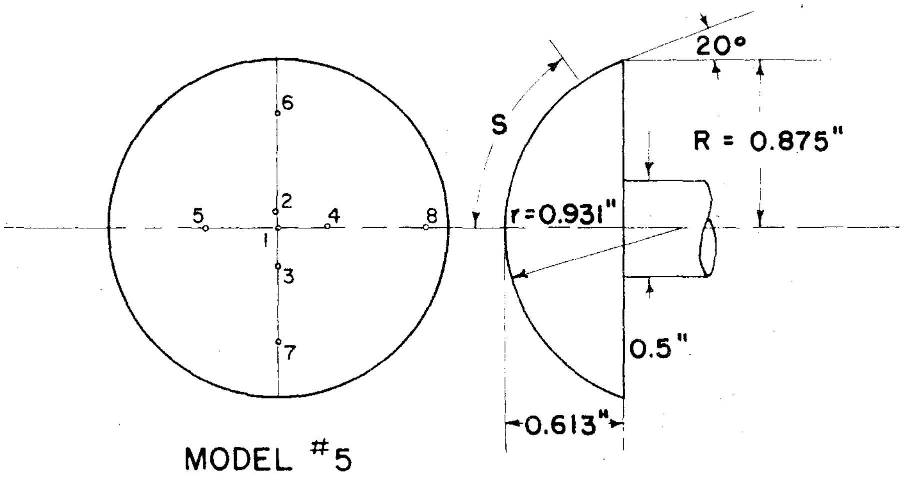

(A) 20° SPHERICAL SEGMENT

r/R = 1.064

Orifice	S(in.)
1	0
2	0.070
3	0.140
4	0.210
5	0.338
6	0.420
7	0.420
8	0.630
9	0.840
10	0.910
11	0.980
12	1.050
13	1.120
14	1.260
15	1.540
16	1.820

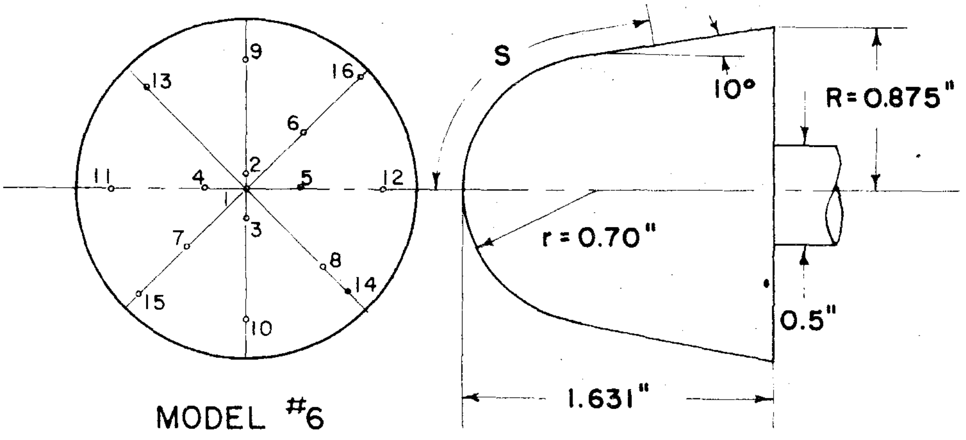

(B) 10° HALF ANGLE CONE

r/R = 0.8

FIG. 5

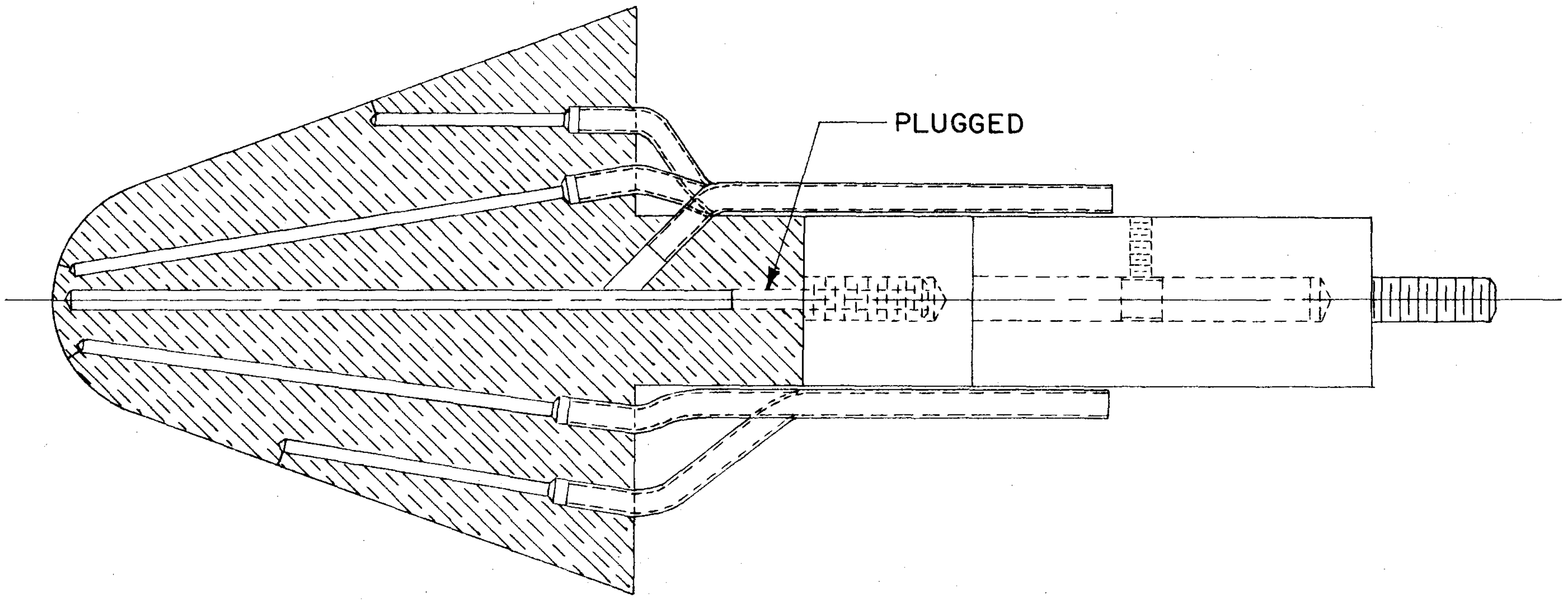

FIG. 6 DETAILS OF TYPICAL MODEL CONSTRUCTION

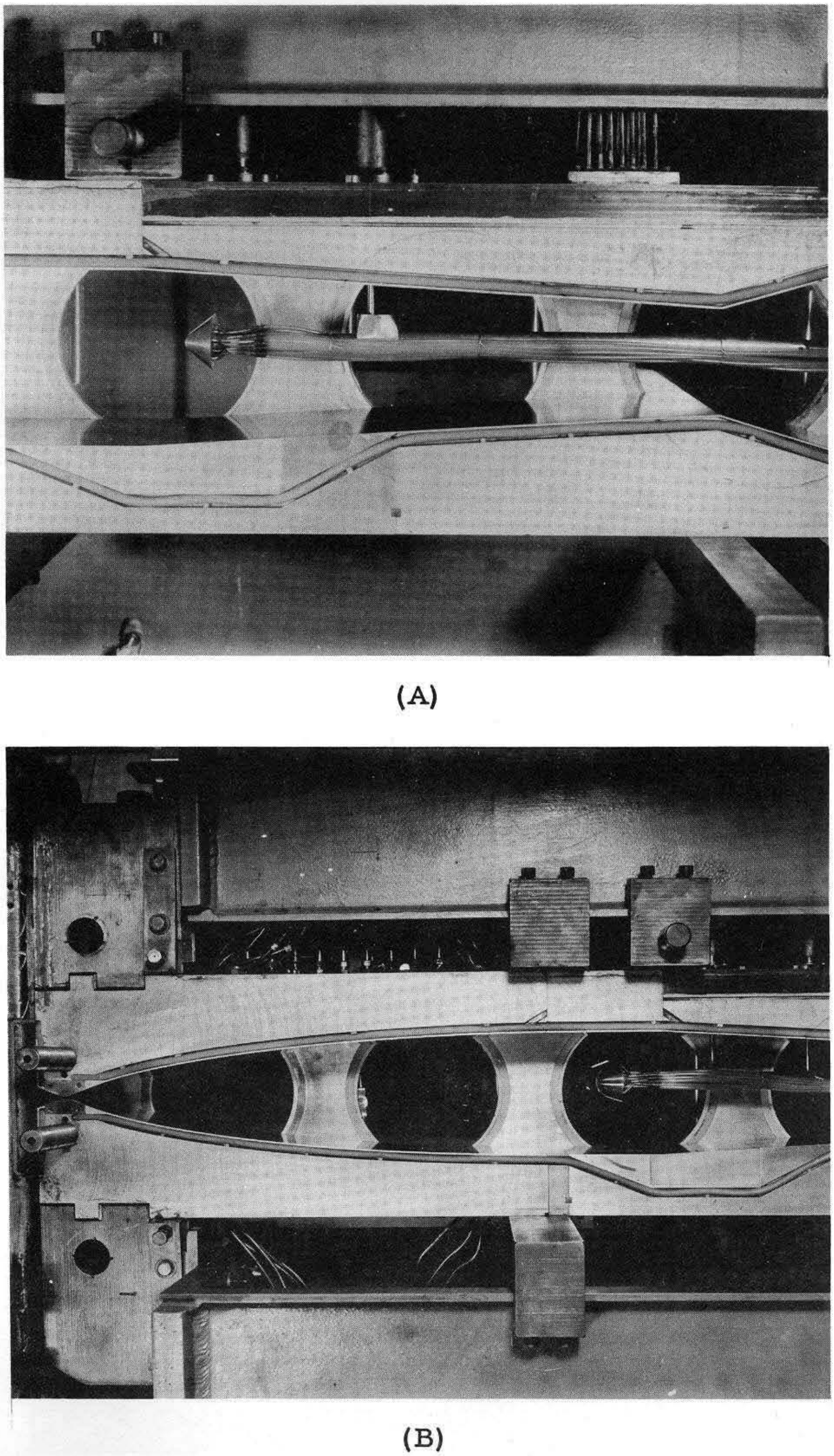

FIG. 7

TEST SECTION OF HYPERSONIC TUNNEL

SHOWING METHODS OF MOUNTING MODELS

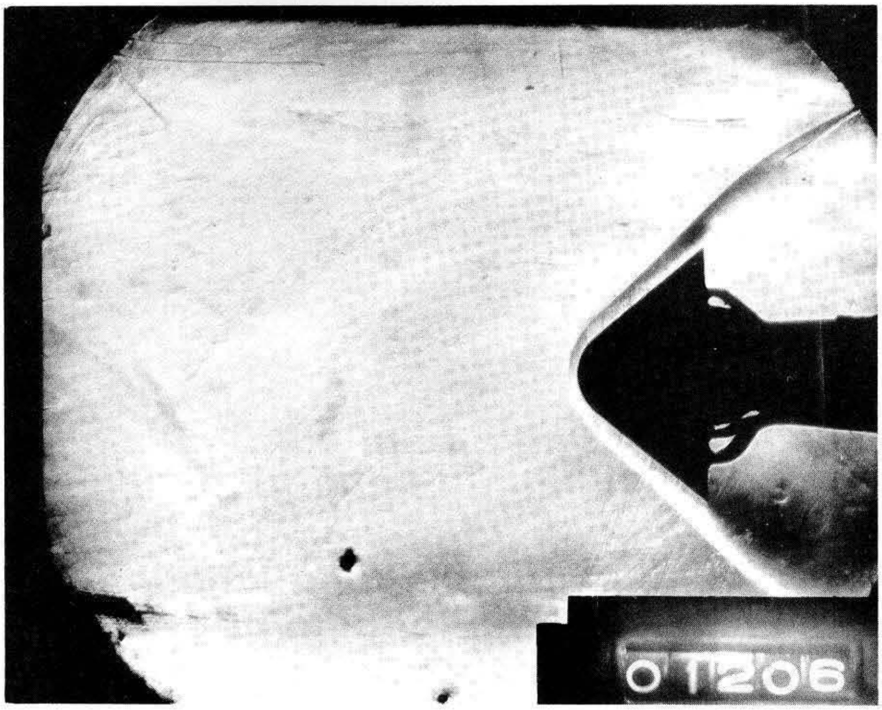

FIG. 8

SCHLIEREN PHOTOGRAPH OF 40° HALF ANGLE CONE

$r/R = 0.4, \alpha = 0^\circ$

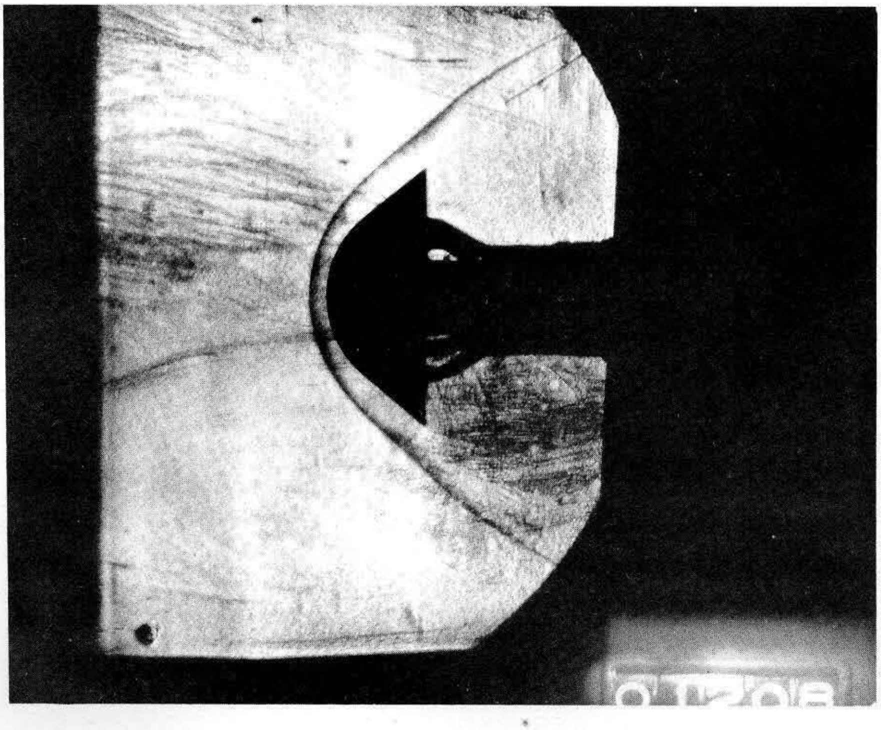

FIG. 9

SCHLIEREN PHOTOGRAPH OF 40° HALF ANGLE CONE

$r/R = 0.8, \alpha = 0^\circ$

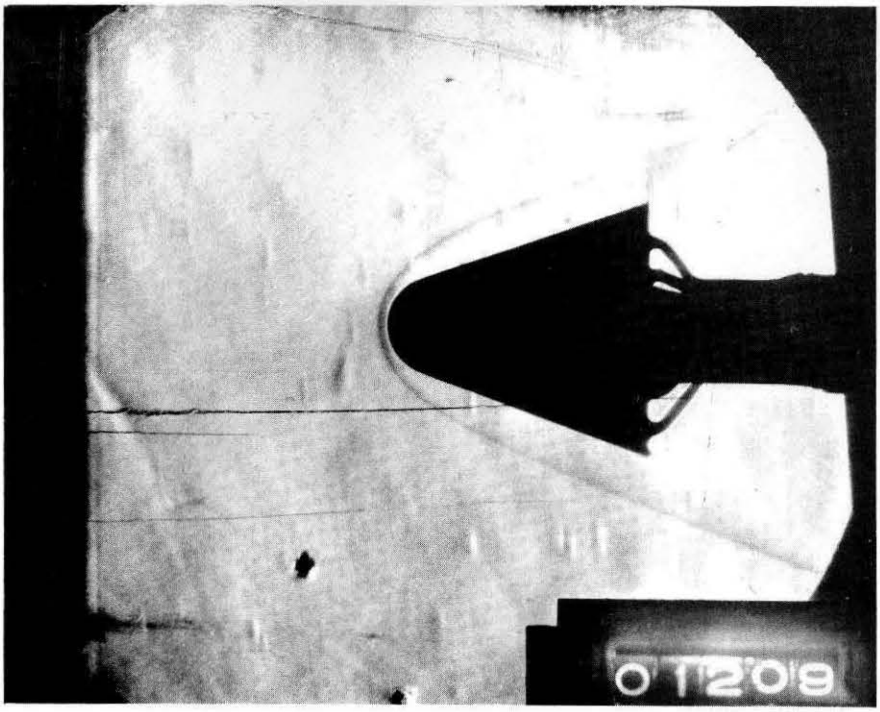

FIG. 10

SCHLIEREN PHOTOGRAPH OF 20° HALF ANGLE CONE

$r/R = 0.4, \alpha = 0^\circ$

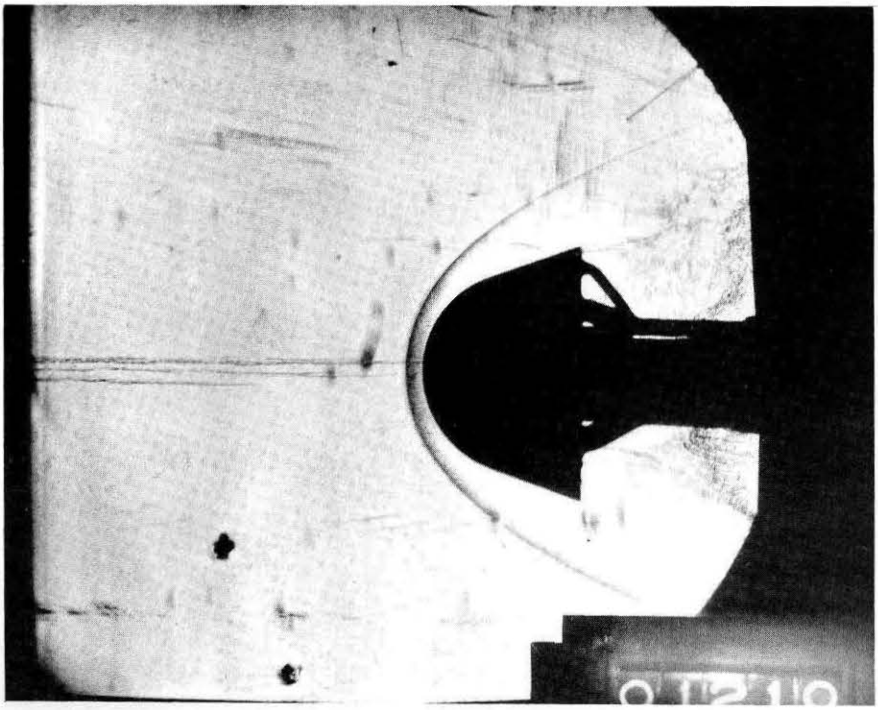

FIG. 11

SCHLIEREN PHOTOGRAPH OF 20° HALF ANGLE CONE

$r/R = 0.8, \alpha = 0^\circ$

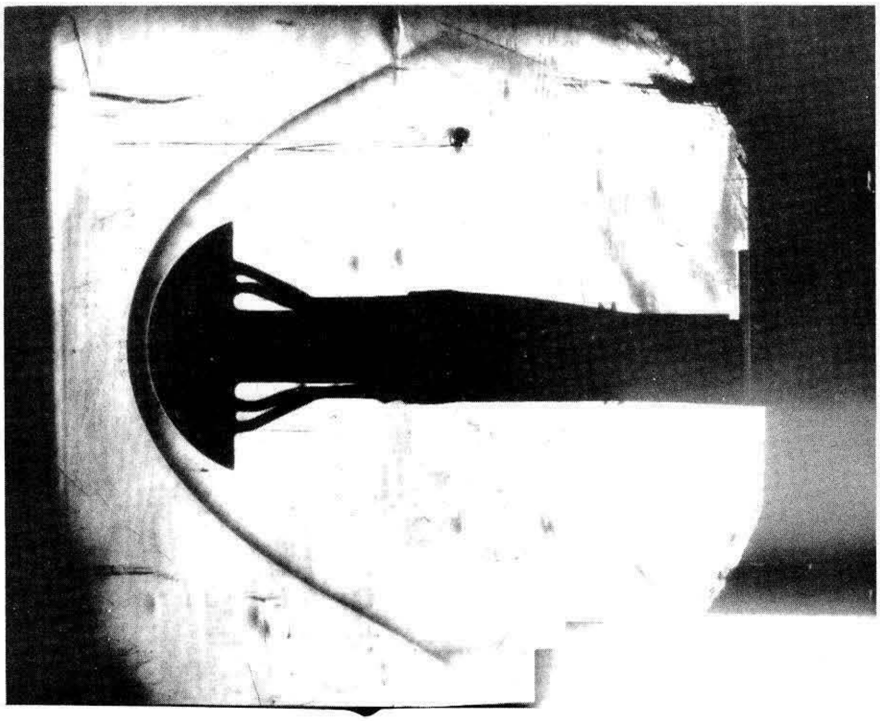

FIG. 12

SCHLIEREN PHOTOGRAPH OF 20° SPHERICAL SECTION

$r/R = 1.064, \alpha = 0^{\circ}$

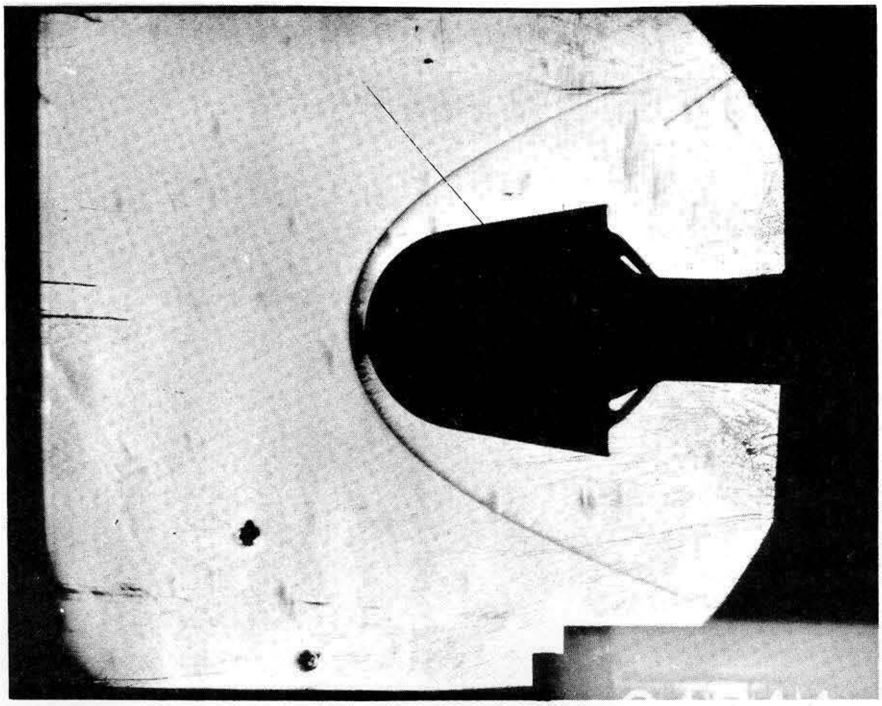

FIG. 13

SCHLIEREN PHOTOGRAPH OF 10° HALF ANGLE CONE

$r/R = 0.8, \alpha = 0^{\circ}$

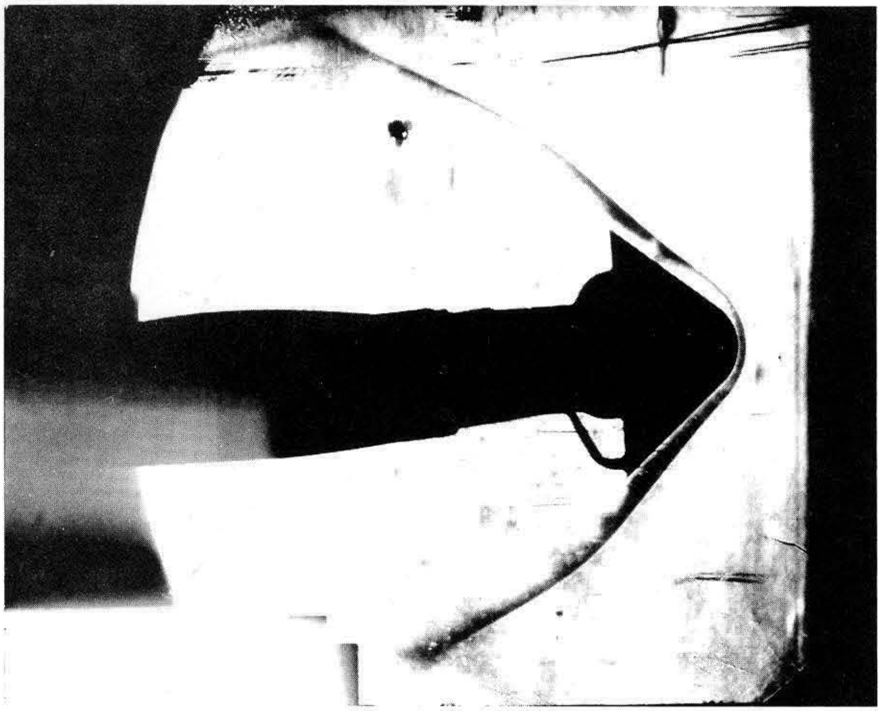

FIG. 14

SCHLIEREN PHOTOGRAPH OF 40° HALF ANGLE CONE

$r/R = 0.4$, $\alpha = 4°$

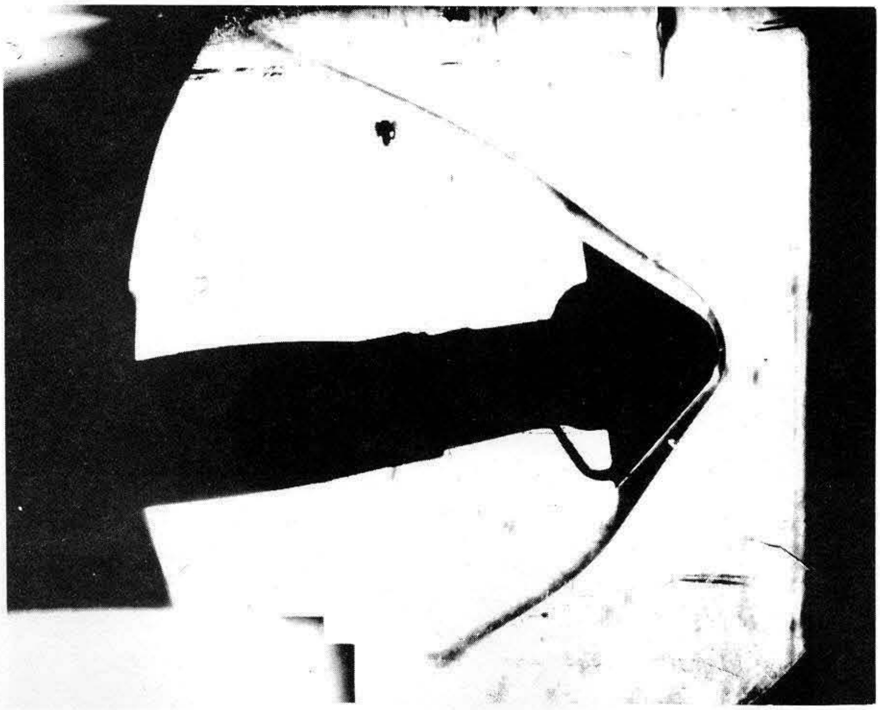

FIG. 15

SCHLIEREN PHOTOGRAPH OF 40° HALF ANGLE CONE

$r/R = 0.4$, $\alpha = 8°$

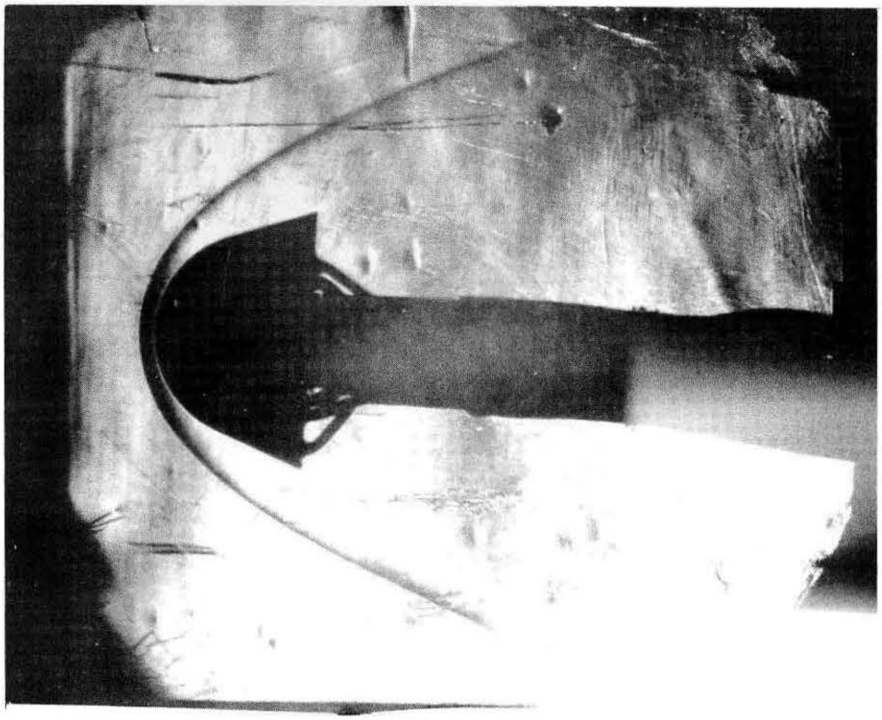

FIG. 16

SCHLIEREN PHOTOGRAPH OF 20° HALF ANGLE CONE

$r/R = 0.8,\ \alpha = 4^\circ$

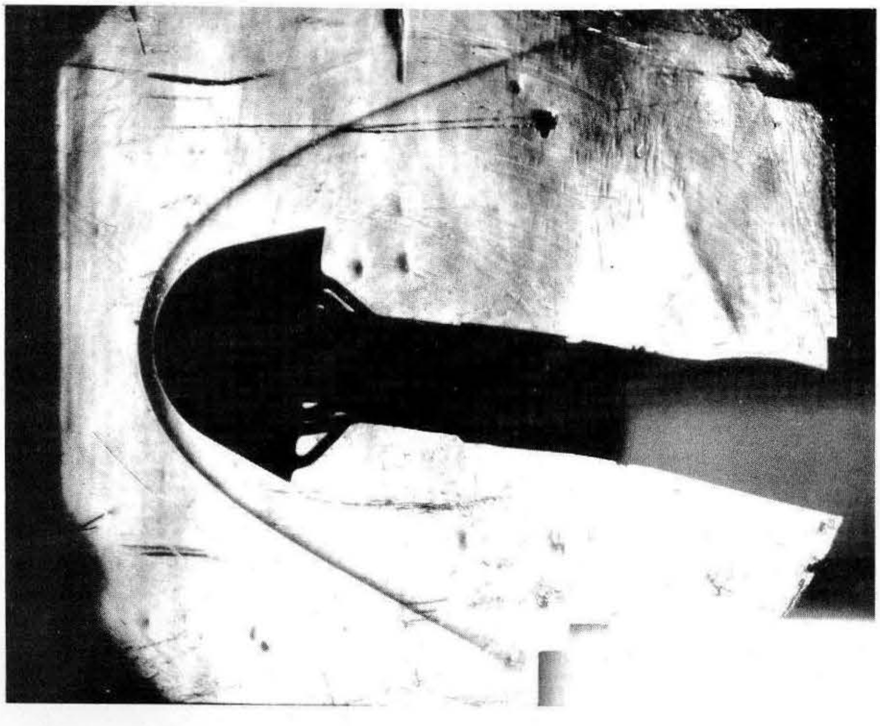

FIG. 17

SCHLIEREN PHOTOGRAPH OF 20° HALF ANGLE CONE

$r/R = 0.8,\ \alpha = 8^\circ$

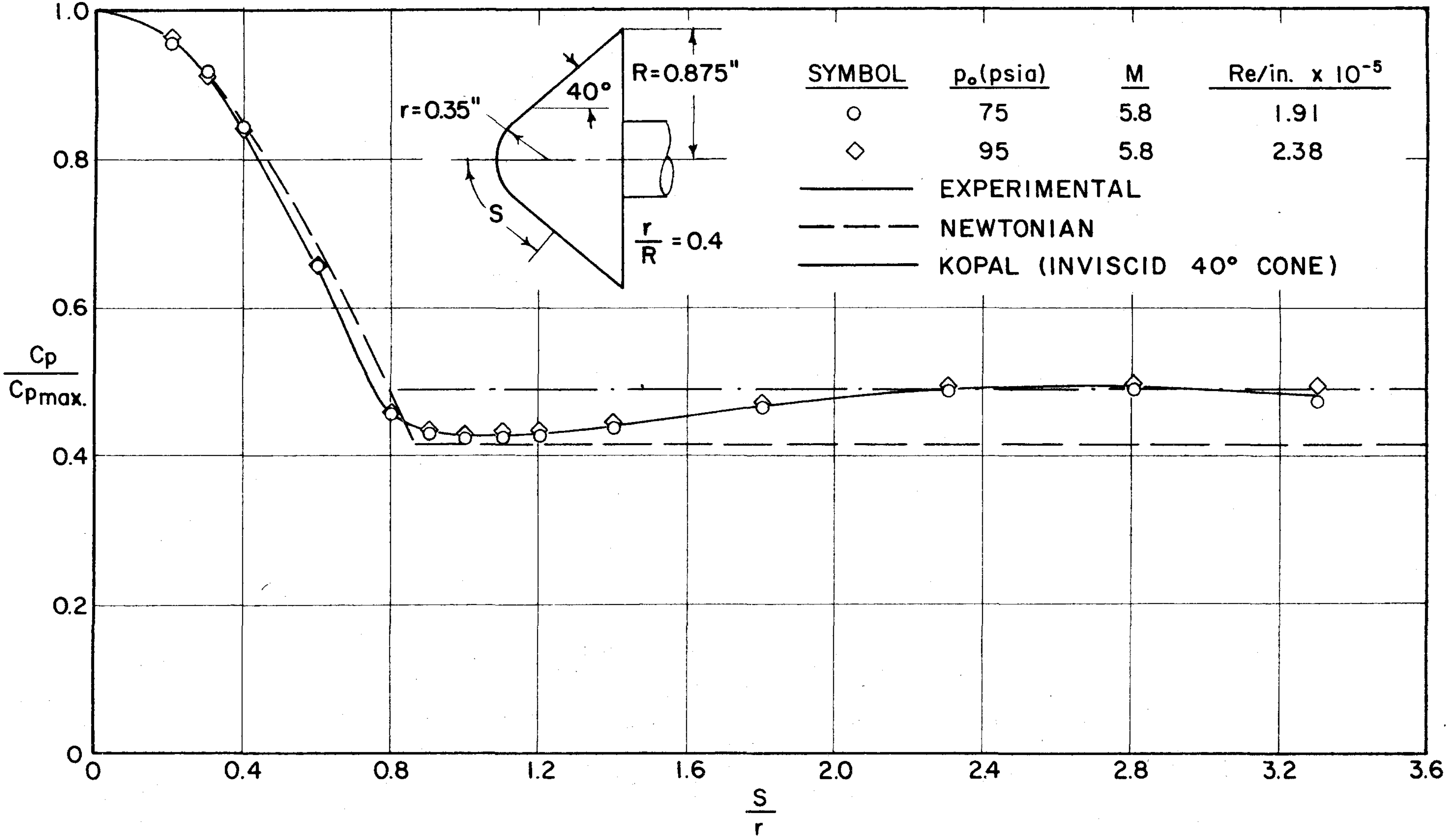

FIG. 18 SURFACE PRESSURE DISTRIBUTION, $\alpha = 0°$

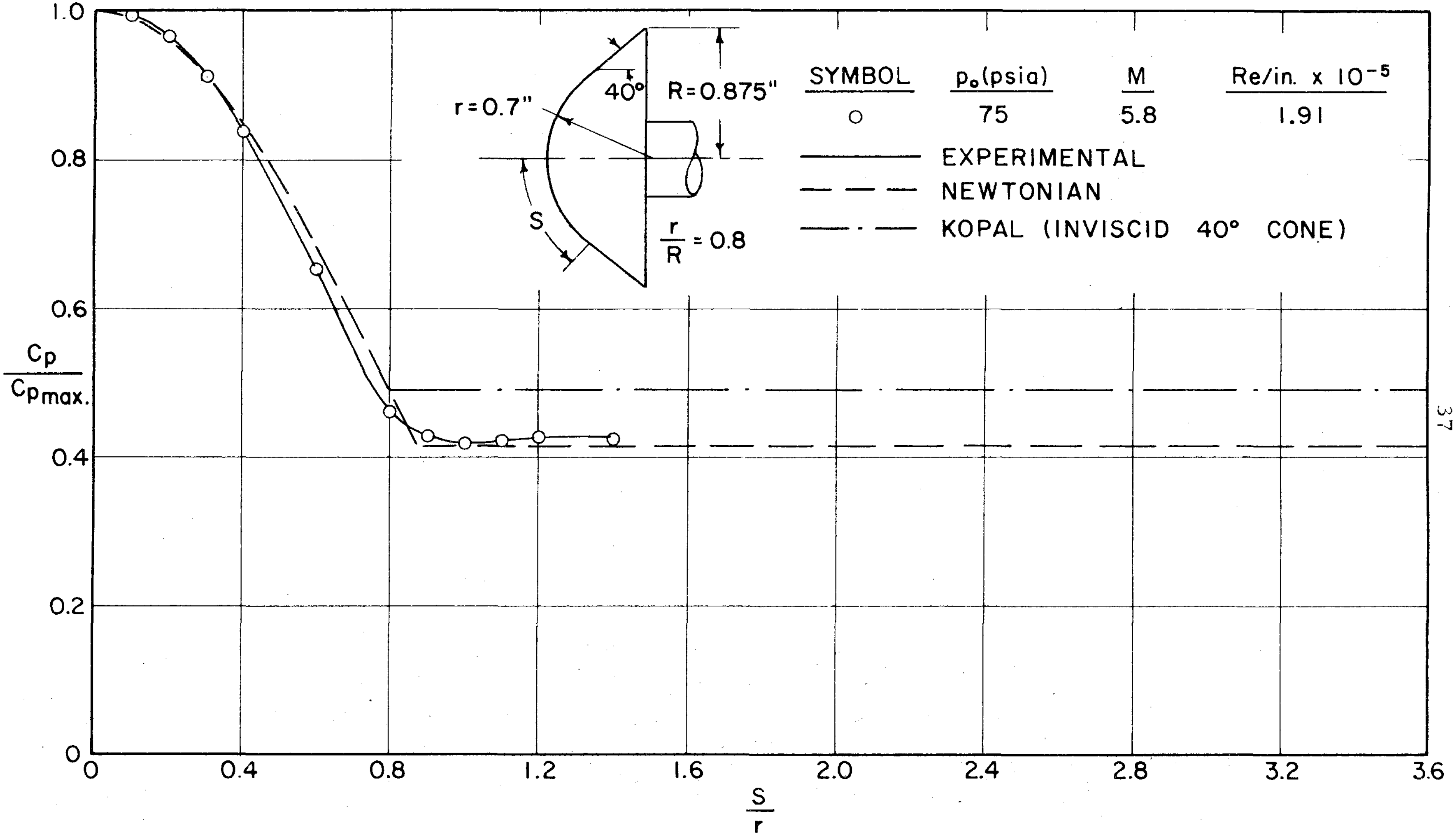

FIG. 19 SURFACE PRESSURE DISTRIBUTION, $\alpha = 0°$

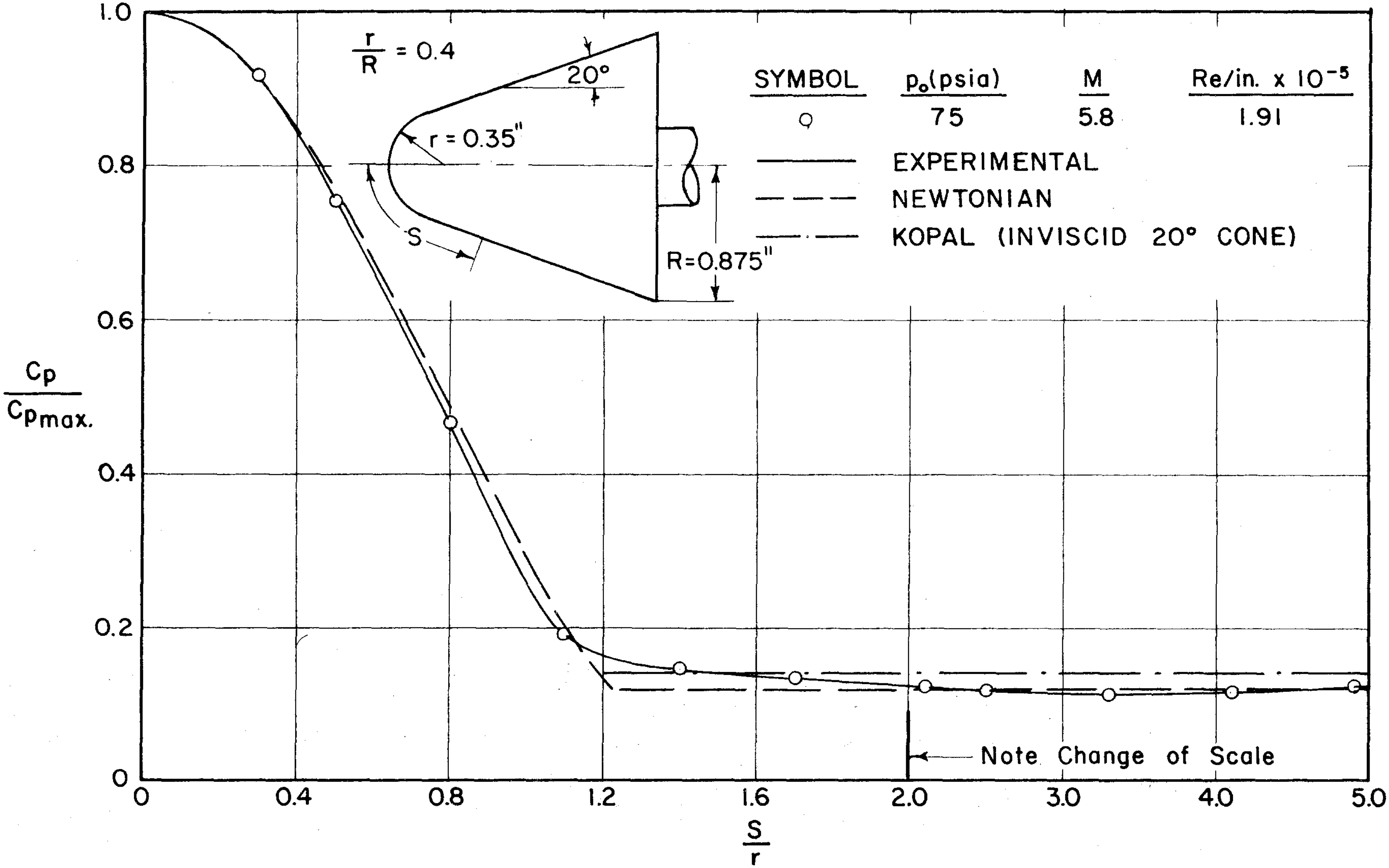

FIG. 20 SURFACE PRESSURE DISTRIBUTION, $\alpha = 0°$

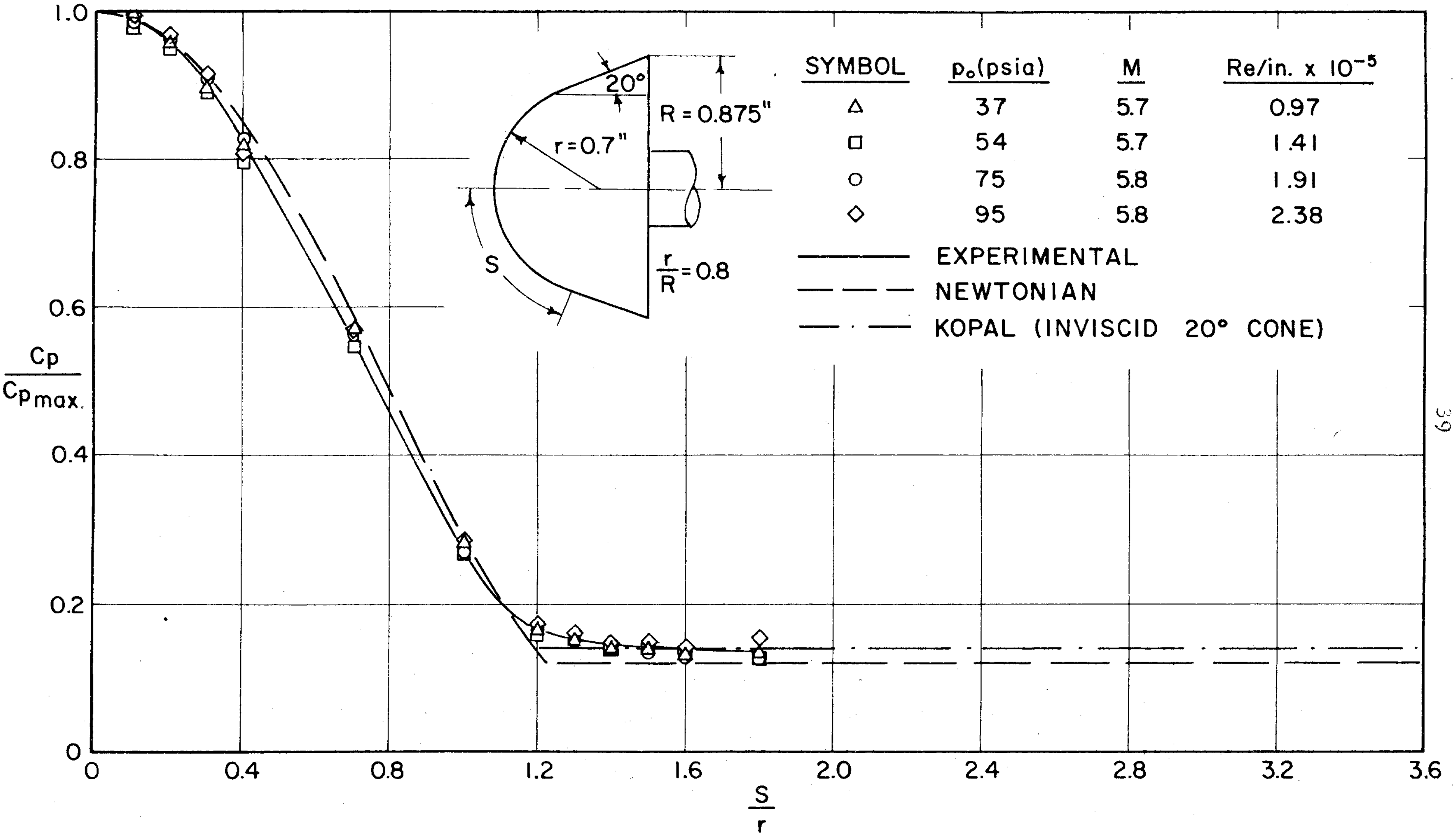

FIG. 21 SURFACE PRESSURE DISTRIBUTION, $\alpha = 0°$

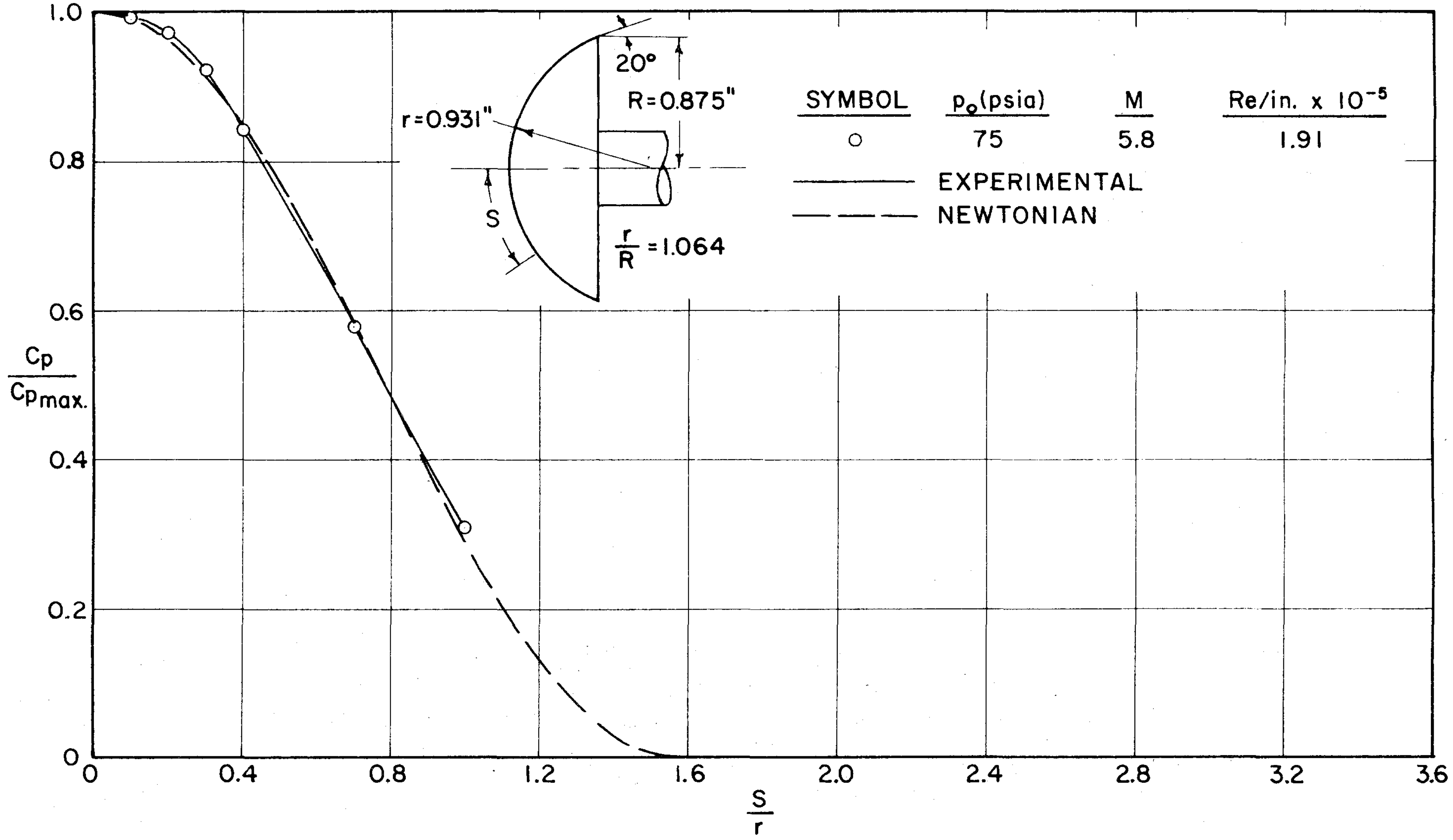

FIG. 22 SURFACE PRESSURE DISTRIBUTION, $\alpha = 0°$

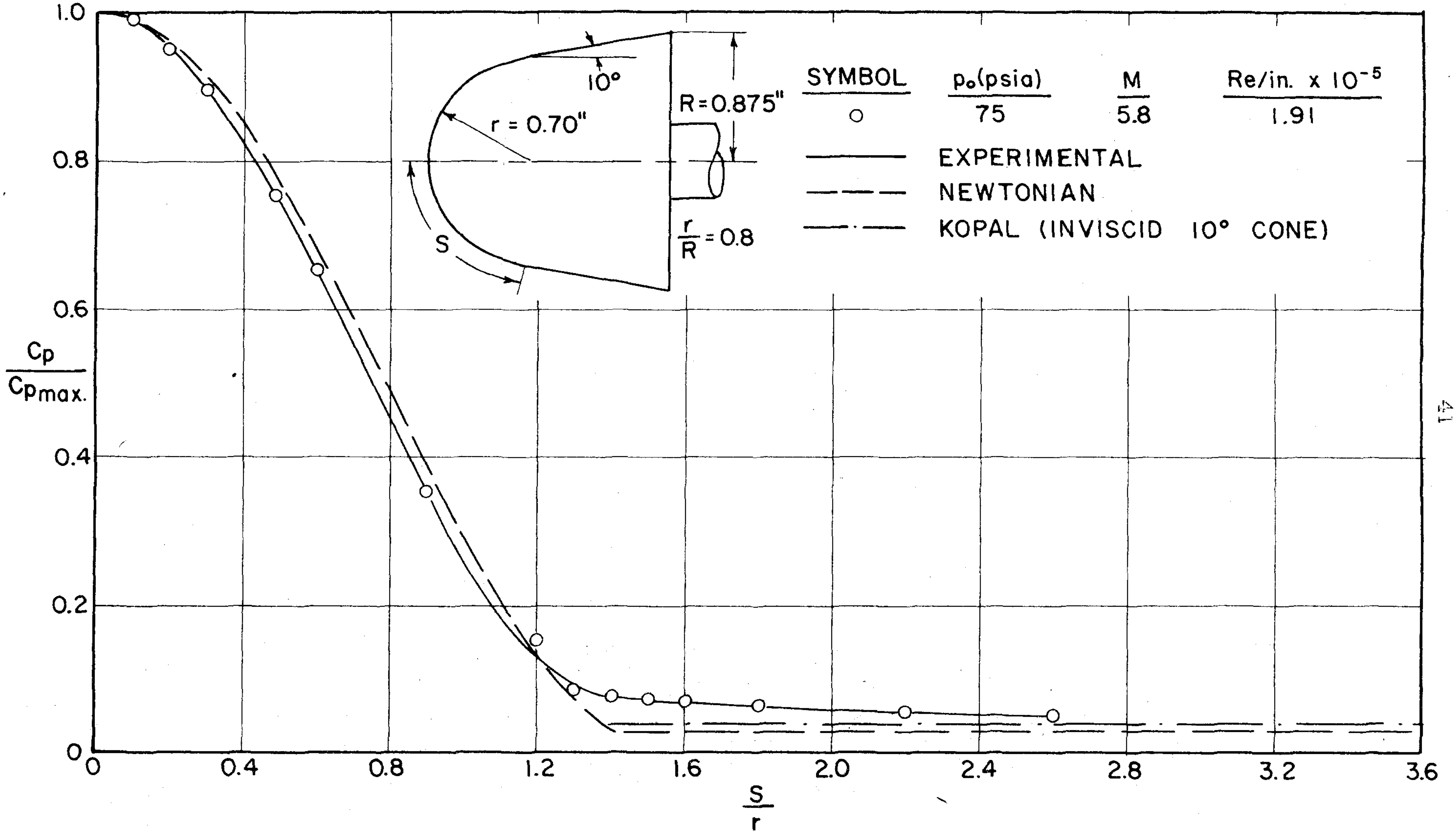

FIG. 23 SURFACE PRESSURE DISTRIBUTION, $\alpha = 0°$

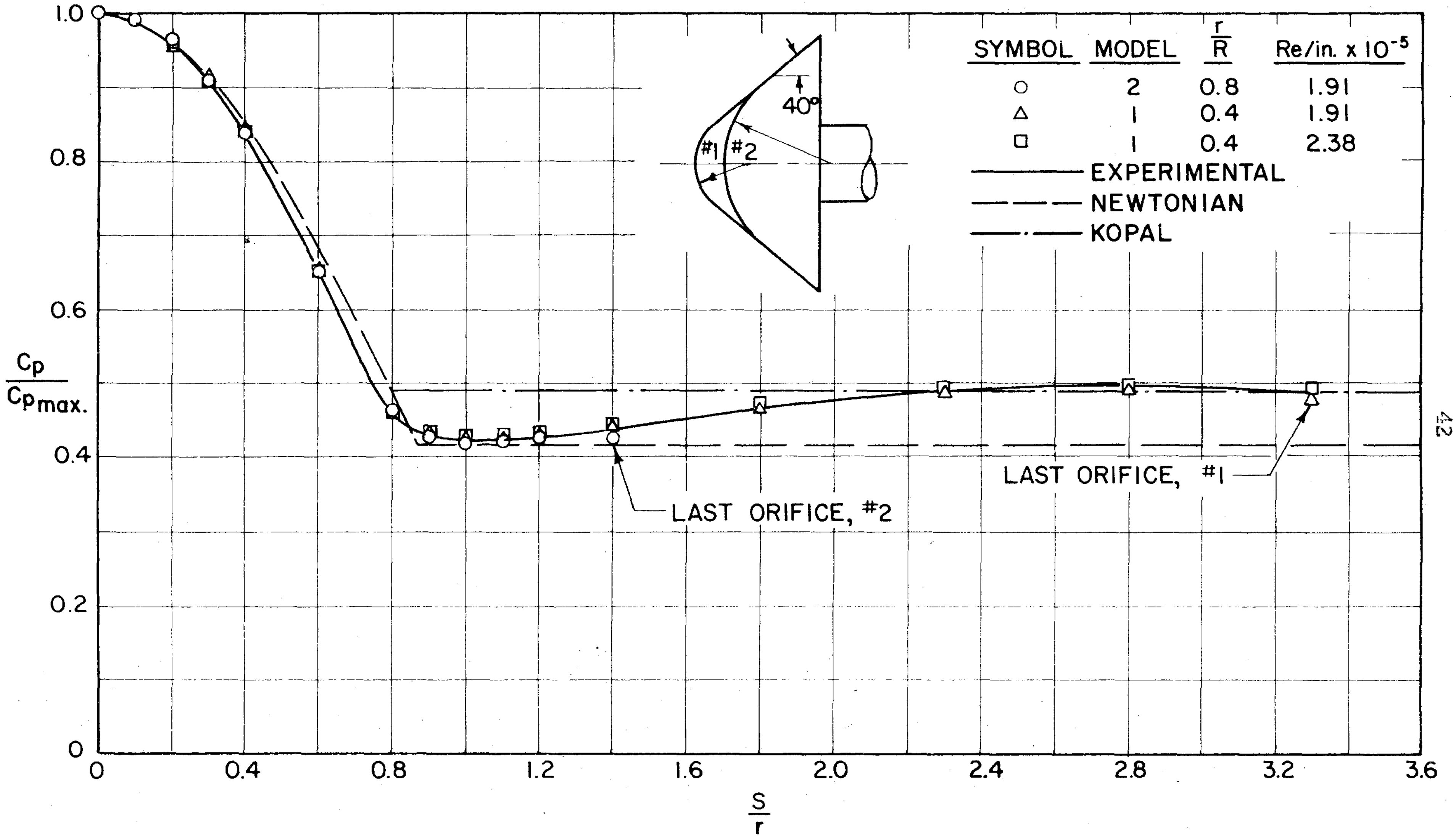

FIG. 24 SURFACE PRESSURE, $\alpha = 0°$

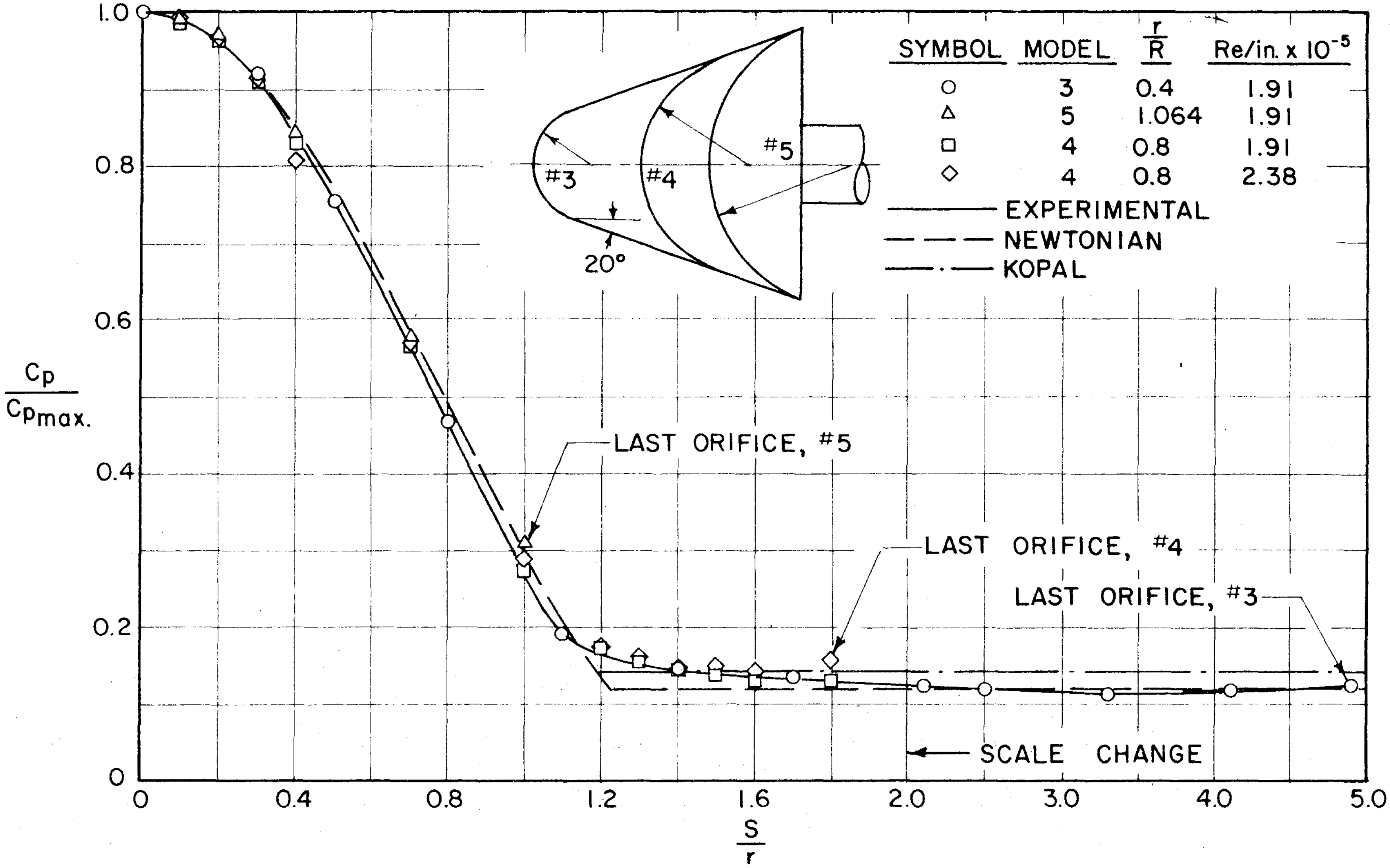

FIG. 25 SURFACE PRESSURE, $\alpha = 0°$

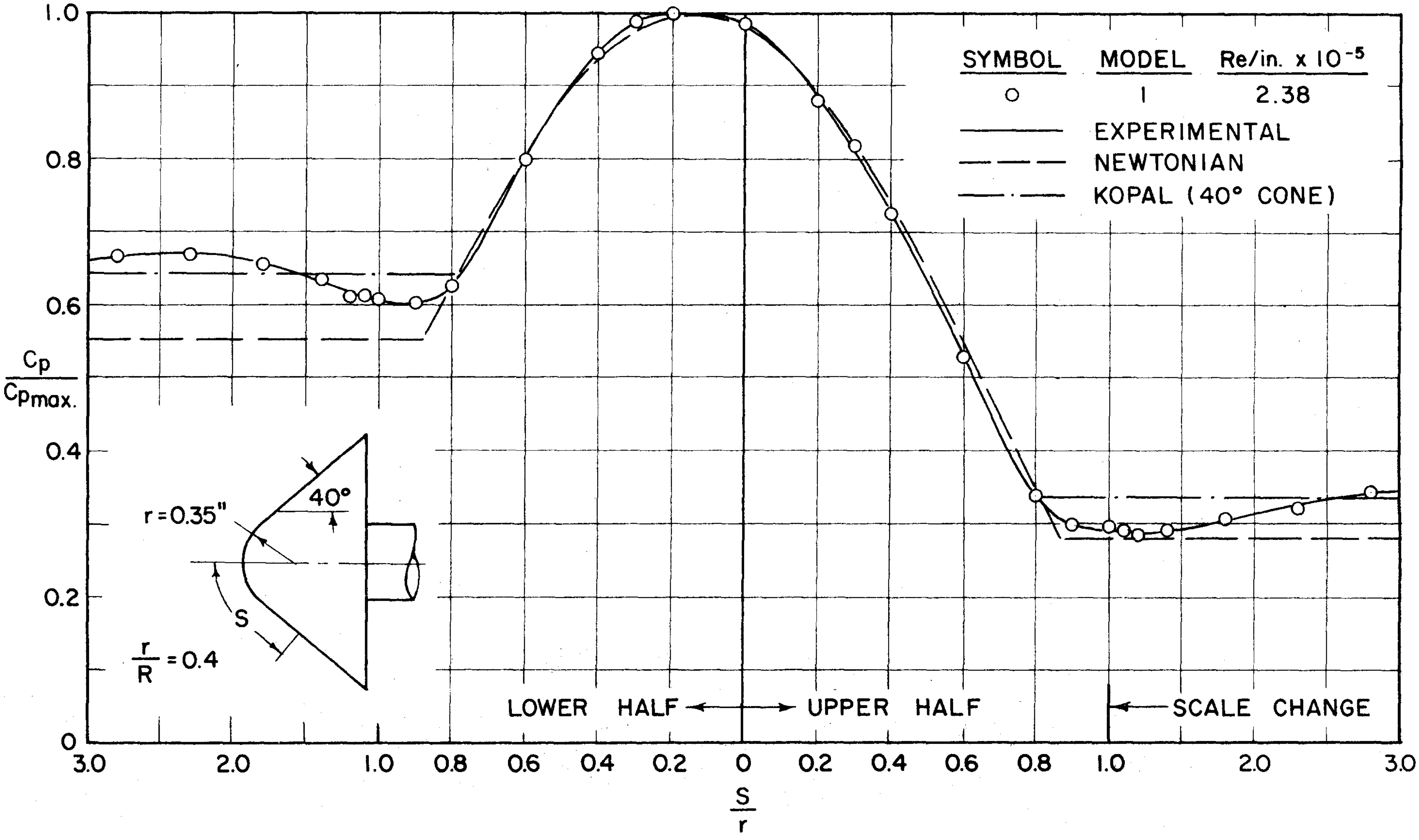

FIG. 26 SURFACE PRESSURE, VERTICAL MERIDIAN PLANE, $\alpha = 8°$

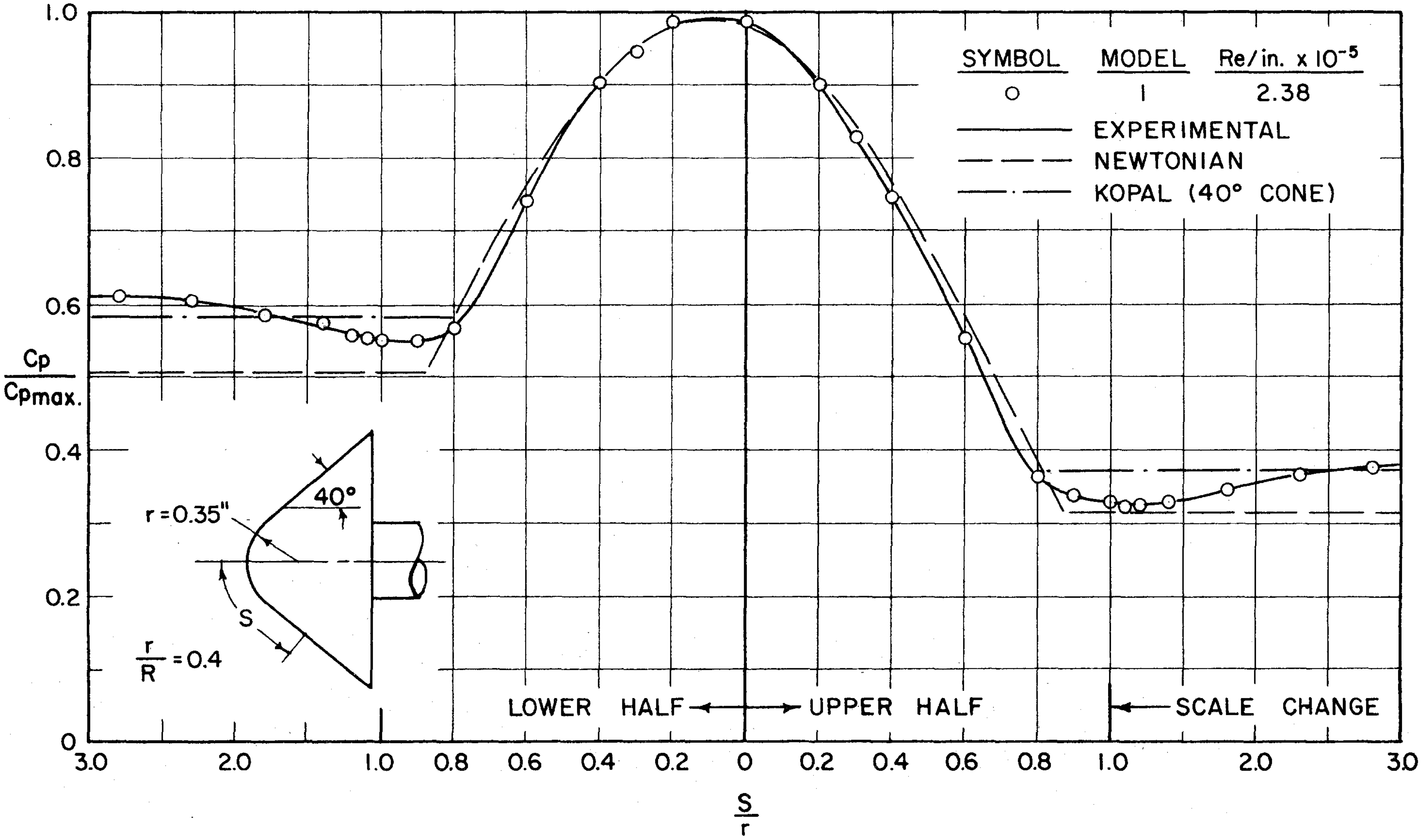

FIG. 27 SURFACE PRESSURE, DIAGONAL MERIDIAN PLANES, $\alpha = 8°$

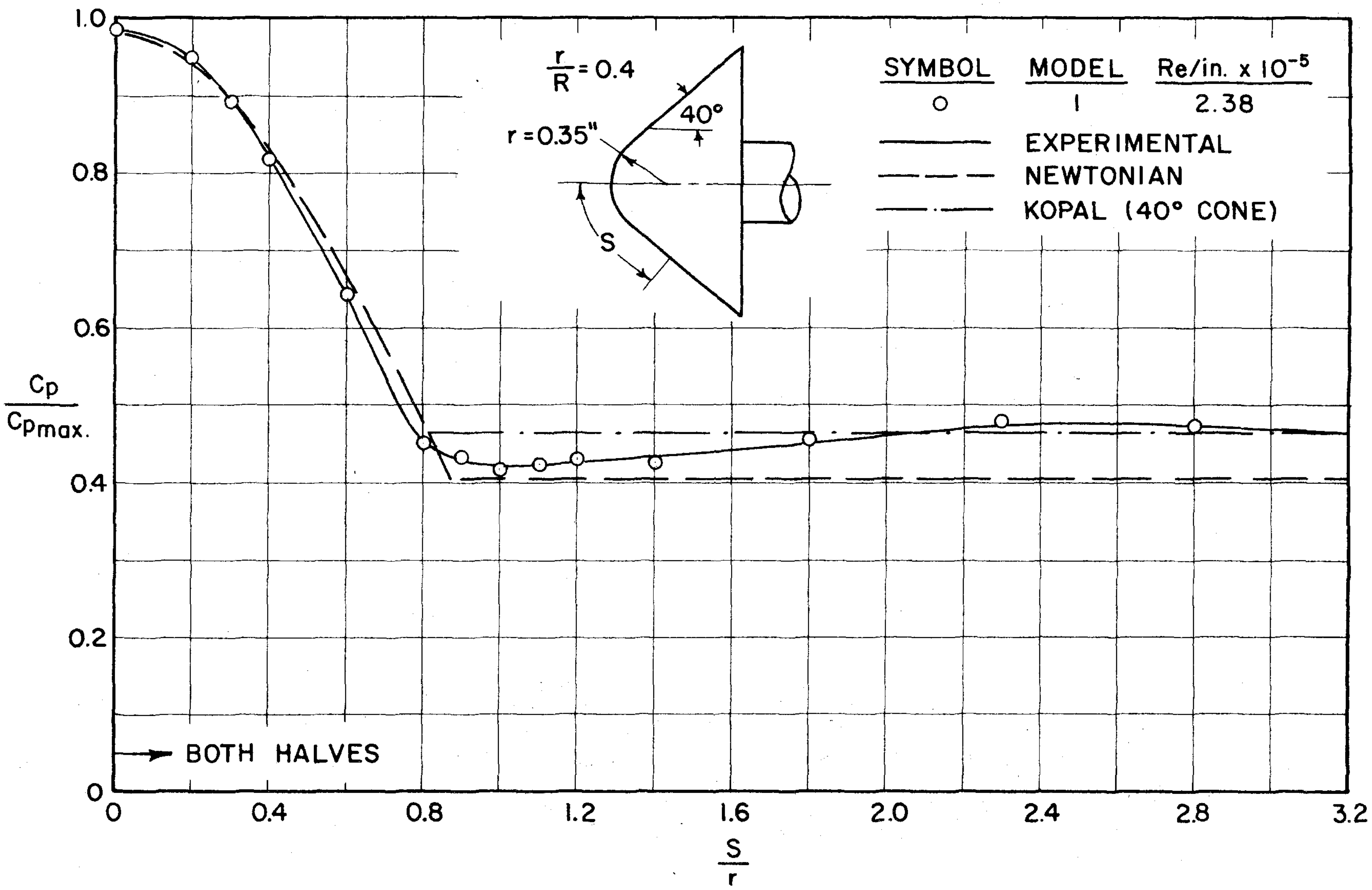

FIG. 28 SURFACE PRESSURE, HORIZONTAL MERIDIAN PLANE, $\alpha = 8°$

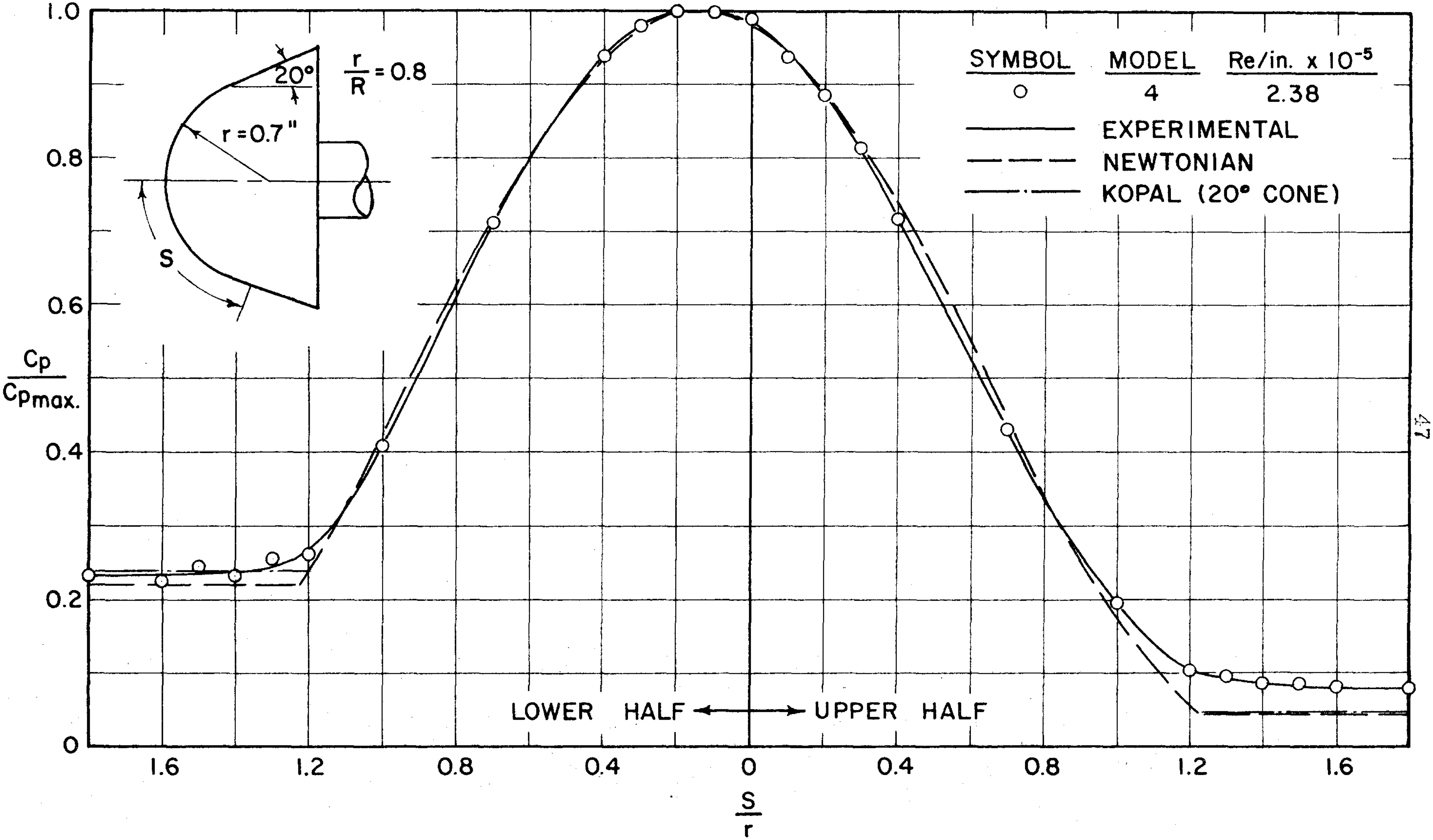

FIG. 29 SURFACE PRESSURE, VERTICAL MERIDIAN PLANE, $\alpha = 8°$

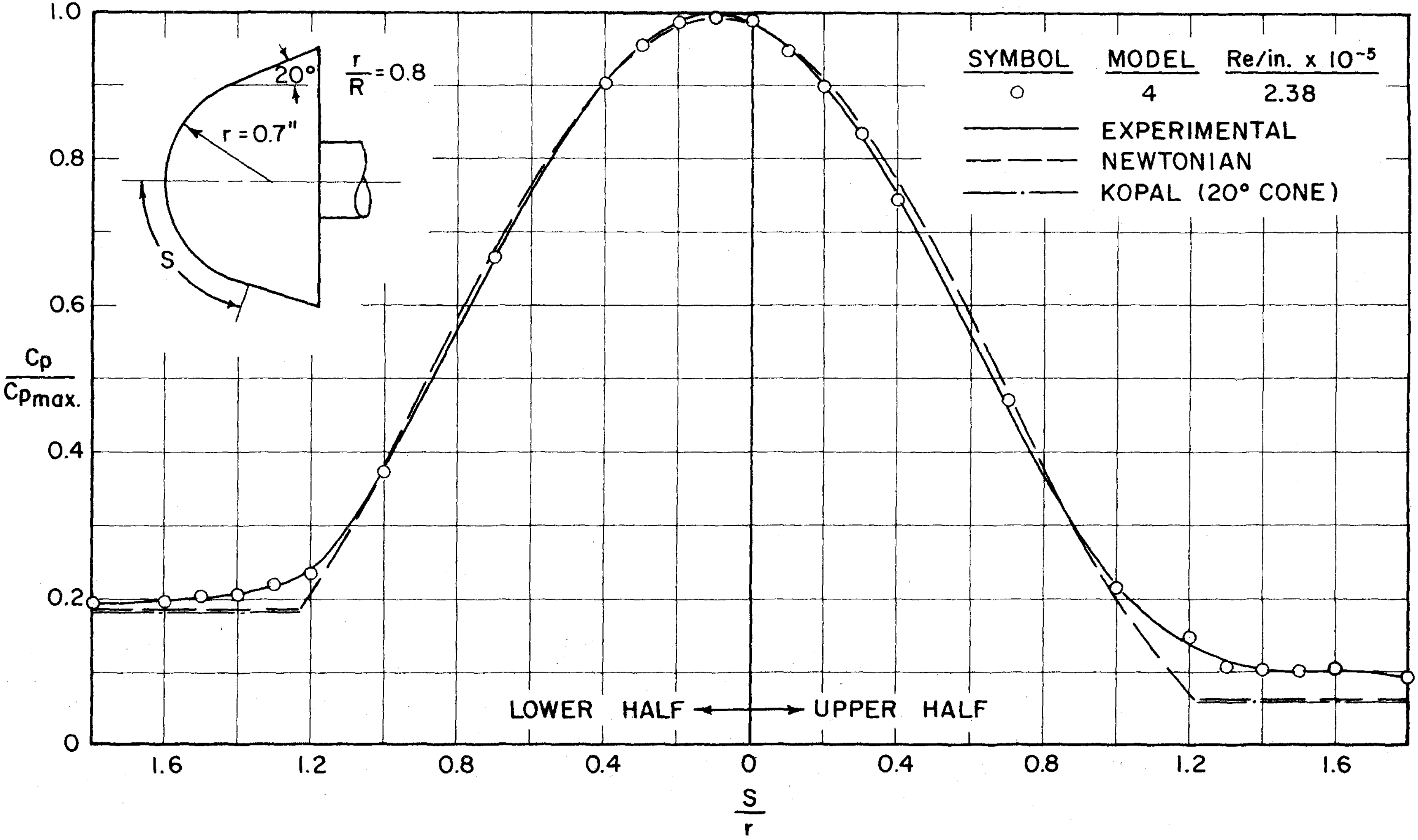

FIG. 30 SURFACE PRESSURE, DIAGONAL MERIDIAN PLANES, α = 8°

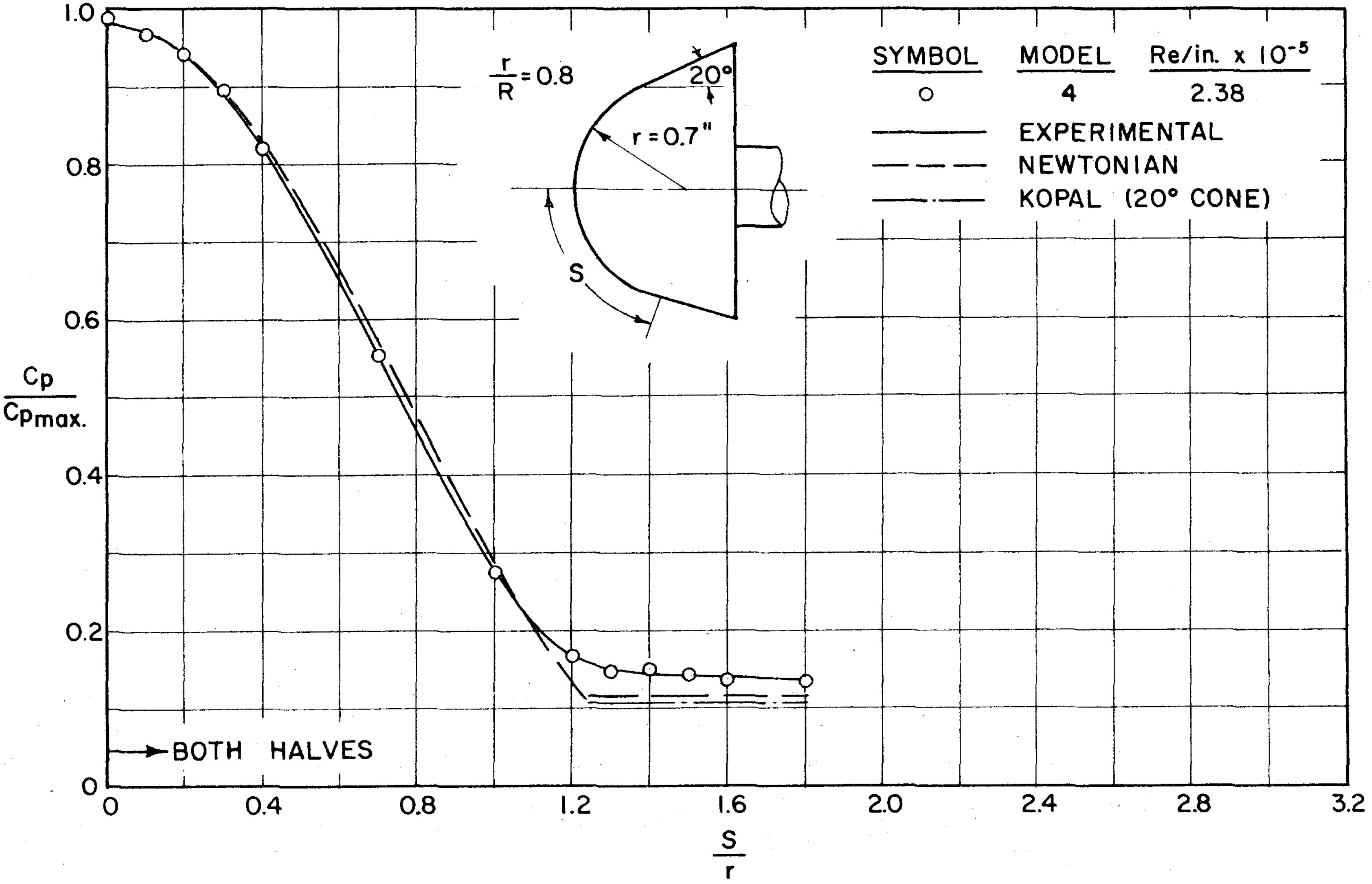

FIG. 31 SURFACE PRESSURE, HORIZONTAL MERIDIAN PLANE, $\alpha = 8°$

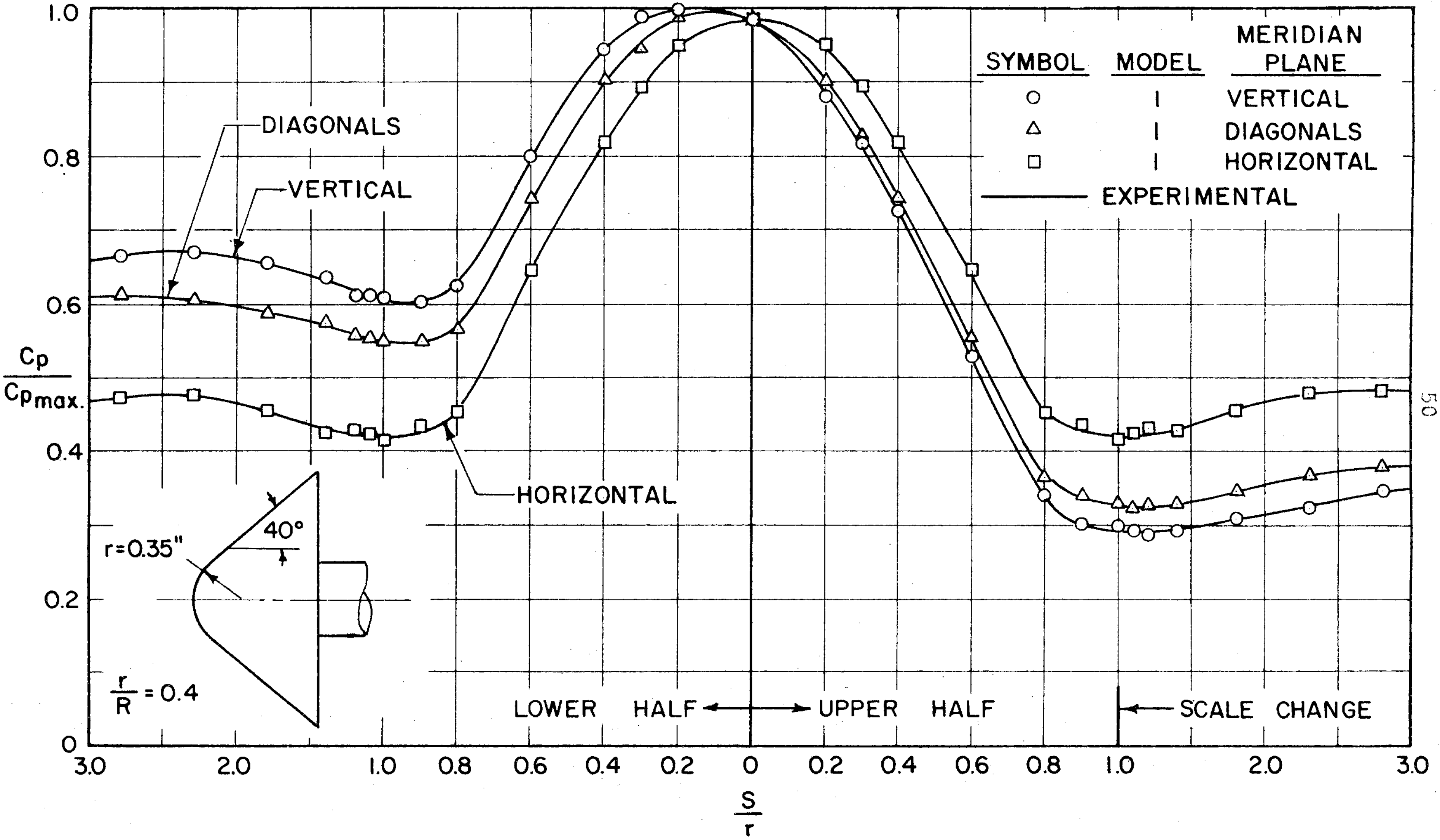

FIG. 32 SURFACE PRESSURE, FOUR MERIDIAN PLANES, $\alpha = 8°$

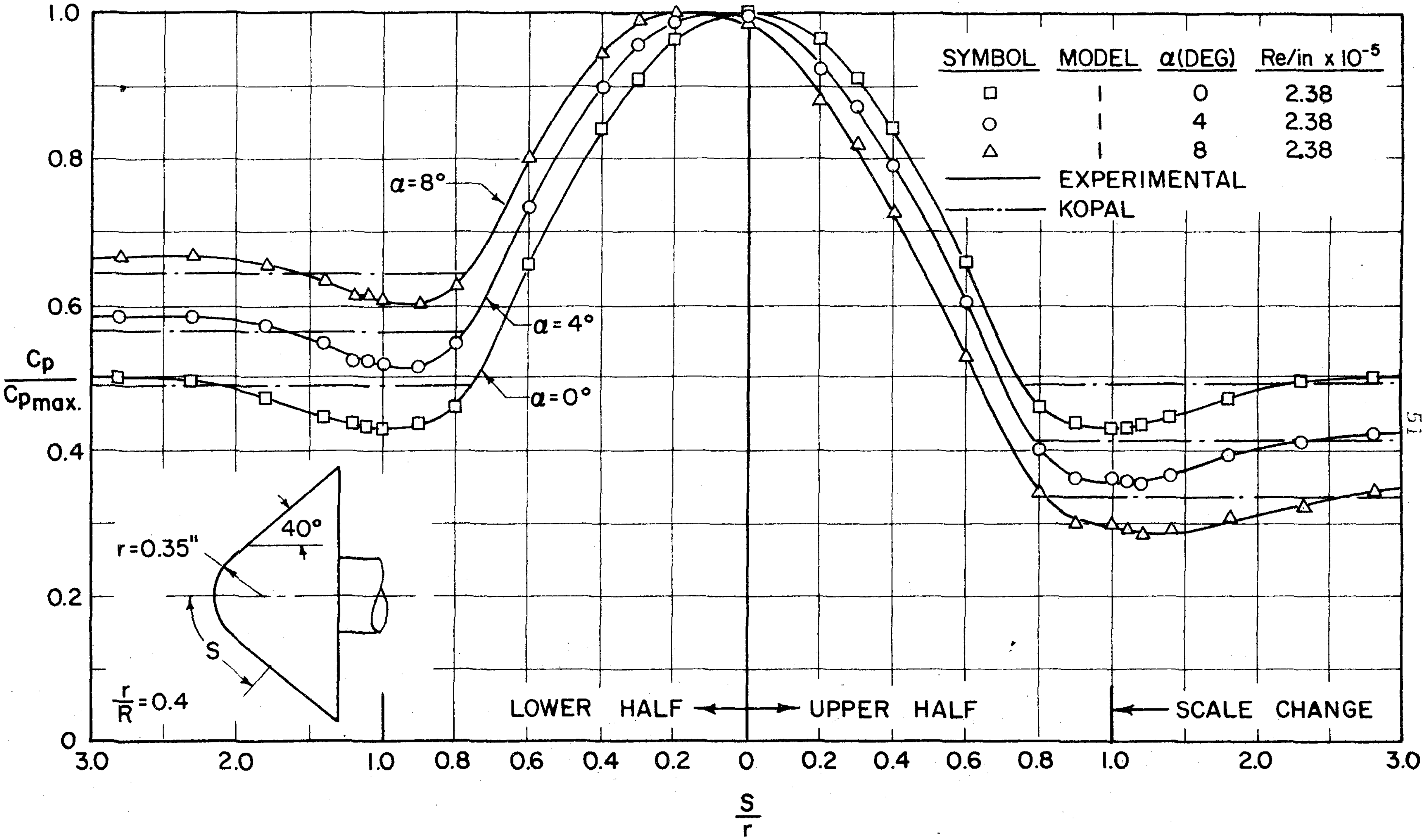

FIG. 33 SURFACE PRESSURE, VERTICAL MERIDIAN PLANE, α = 0°, 4°, 8°

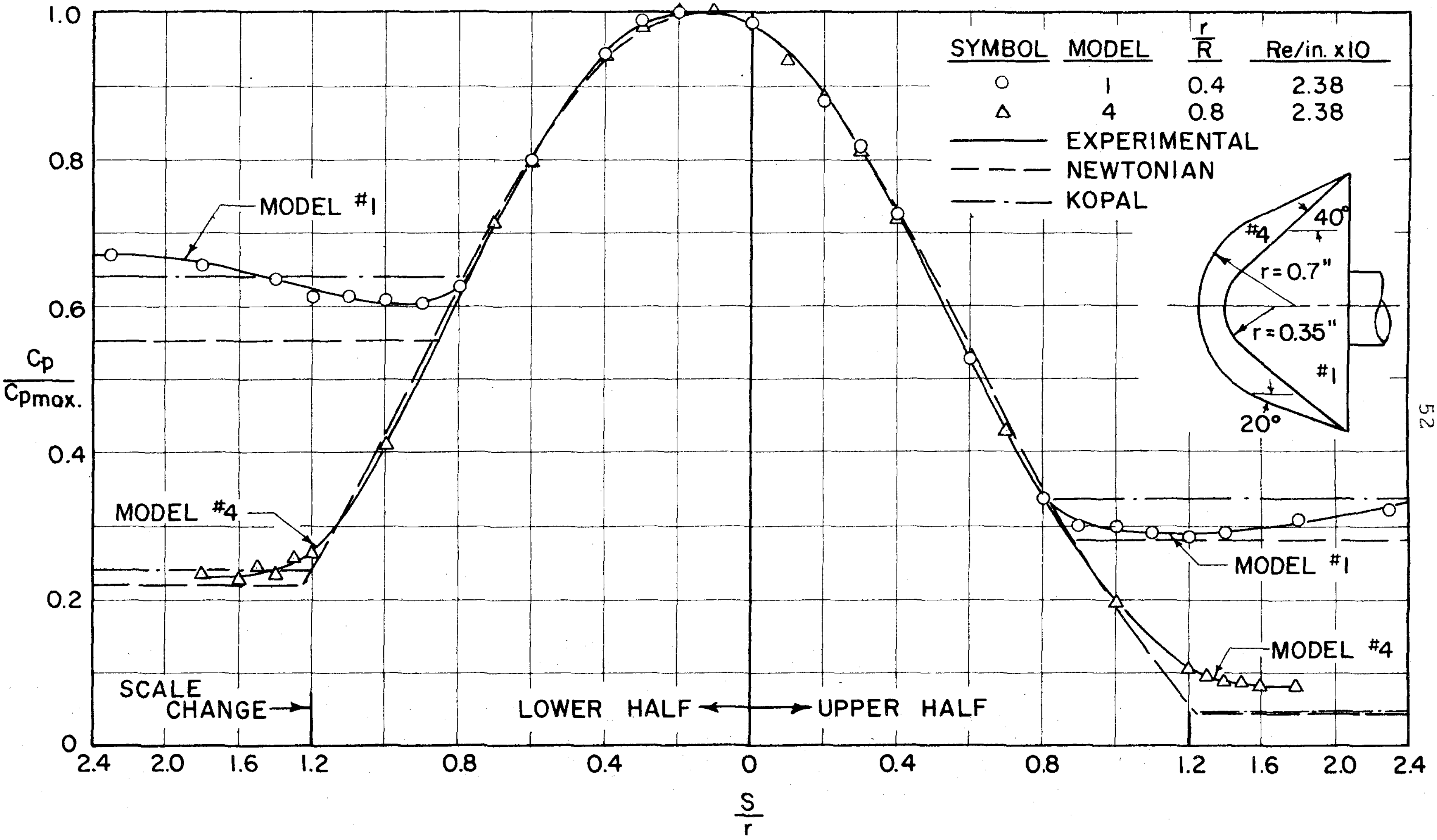

FIG. 34 SURFACE PRESSURE, VERTICAL MERIDIAN PLANE, $\alpha = 8°$

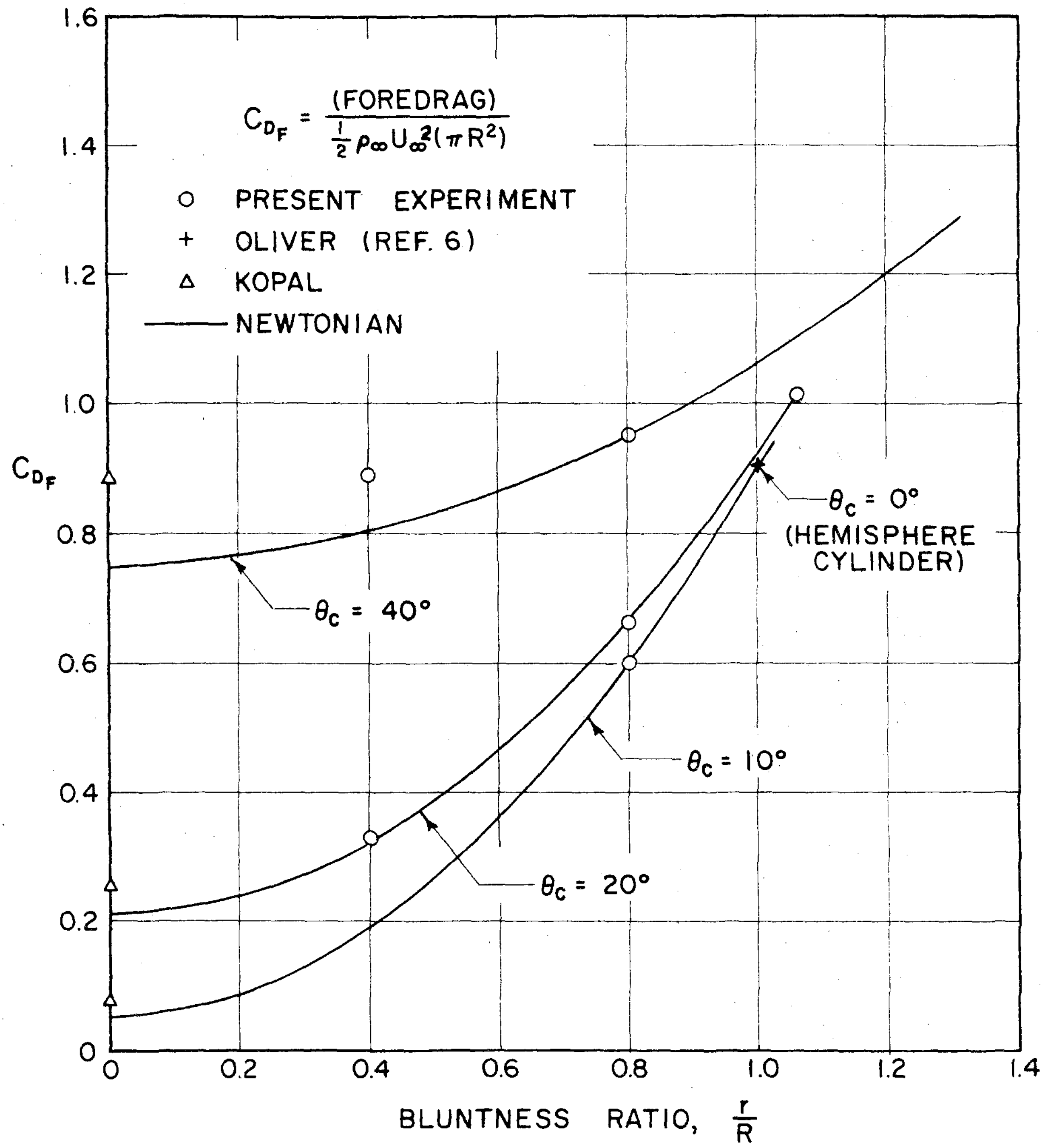

PRESSURE FOREDRAG OF SPHERICAL NOSED CONES AT MACH NUMBER 5.8

FIG. 35